

Review

# Optimization Methods of Tungsten Oxide-Based Nanostructures as Electrocatalysts for Water Splitting

Yange Wang, Rongming Wang \*  and Sibin Duan \* 

Beijing Advanced Innovation Center for Materials Genome Engineering,  
Beijing Key Laboratory for Magneto-Photoelectrical Composite and Interface Science,  
State Key Laboratory for Advanced Metals and Materials, School of Mathematics and Physics,  
University of Science and Technology Beijing, Beijing 100083, China

\* Correspondence: rmwang@ustb.edu.cn (R.W.); sibinduan@ustb.edu.cn (S.D.)

**Abstract:** Electrocatalytic water splitting, as a sustainable, pollution-free and convenient method of hydrogen production, has attracted the attention of researchers. However, due to the high reaction barrier and slow four-electron transfer process, it is necessary to develop and design efficient electrocatalysts to promote electron transfer and improve reaction kinetics. Tungsten oxide-based nanomaterials have received extensive attention due to their great potential in energy-related and environmental catalysis. To maximize the catalytic efficiency of catalysts in practical applications, it is essential to further understand the structure–property relationship of tungsten oxide-based nanomaterials by controlling the surface/interface structure. In this review, recent methods to enhance the catalytic activities of tungsten oxide-based nanomaterials are reviewed, which are classified into four strategies: morphology regulation, phase control, defect engineering, and heterostructure construction. The structure–property relationship of tungsten oxide-based nanomaterials affected by various strategies is discussed with examples. Finally, the development prospects and challenges in tungsten oxide-based nanomaterials are discussed in the conclusion. We believe that this review provides guidance for researchers to develop more promising electrocatalysts for water splitting.

**Keywords:** tungsten oxide; electrocatalysis; structure–property relationship; water splitting



**Citation:** Wang, Y.; Wang, R.; Duan, S. Optimization Methods of Tungsten Oxide-Based Nanostructures as Electrocatalysts for Water Splitting. *Nanomaterials* **2023**, *13*, 1727. <https://doi.org/10.3390/nano13111727>

Academic Editor: Adriano Sacco

Received: 29 April 2023

Revised: 19 May 2023

Accepted: 23 May 2023

Published: 25 May 2023



**Copyright:** © 2023 by the authors. Licensee MDPI, Basel, Switzerland. This article is an open access article distributed under the terms and conditions of the Creative Commons Attribution (CC BY) license (<https://creativecommons.org/licenses/by/4.0/>).

## 1. Introduction

With the rapid development of global modernization, the excessive consumption of non-renewable energy sources, such as oil and coal, has resulted in the crisis of greenhouse effect, energy shortage, and severe environmental pollution [1–5]. It is urgent to develop clean and sustainable energy to alleviate energy pressure and ameliorate environmental problems. Therefore, sustainable clean energy resources, such as wind, solar, tidal, and hydropower, have been extensively studied [6–11]. However, these energy sources have the disadvantages of uneven geographical distribution and intermittency, which seriously restrict their popularization and application [12]. Hydrogen fuel is expected to play a significant role in developing sustainable clean energy due to its high energy density, high energy yield (122 kJ/g), and environmentally friendly characteristics [13–15]. However, it is estimated that nearly 96% of worldwide hydrogen comes from the conversion of fossil fuels, where the pollution byproducts cause environmental problems, such as climate warming [14,16–19]. Electrochemical water splitting, as a sustainable method of producing hydrogen with simple operation, mild reaction conditions, environmental protection, and low cost, has attracted much attention from researchers [13,20–22]. The water-splitting process involves two half-reactions, i.e., hydrogen evolution reaction (HER) and oxygen evolution reaction (OER). However, due to the slow-kinetic four-electron transfer process with a high reaction barrier, the potential required for water splitting is always higher than the theoretical decomposition potential of water (1.23 V), resulting in additional electrical power consumption [23,24]. Effective electrocatalysts are required to reduce

the reaction barrier and accelerate the reaction kinetics. Generally speaking, noble metal (Pt, Ir)-based catalysts show ideal electrocatalytic performance due to their appropriate hydrogen adsorption-free energy. However, the scarcity and high prices of noble metals have prevented their widespread application [25,26]. Therefore, it is essential to develop effective catalysts that are affordable, stable, and low in noble metals.

Among all the candidates, tungsten oxide has attracted much attention because of its abundant reserves, affordable price, and great stability. It is worth noting that tungsten oxides are typical n-type semiconductors with band gaps of 2.6–3.0 V [27], which have a variety of morphologies and crystal phases, and they exhibit reversible surface oxygen ion exchange and excellent redox capacity, owing to their oxidation states flexibly converting between  $W^{6+}$ ,  $W^{5+}$ , and  $W^{4+}$  [28–30]. Consequently, tungsten oxide is expected to be a superior substitute for noble metals [29,31]. The fundamental crystal unit of tungsten oxide is  $WO_6$ , an octahedral structure. Tungsten oxide possesses a variety of crystal phases, including tetragonal, orthorhombic, monoclinic I, hexagonal, triclinic, and monoclinic II, due to the varying tilt angles and rotation directions of  $WO_6$  units [30,32]. Notably, the  $WO_6$  octahedral units can form shared angles or shared edges, and the more shared angles/edges there are, the more oxygen vacancies and low valence W species are generated, forming a  $WO_x$  structure with a non-stoichiometric ratio [28,33,34]. The oxygen vacancy is accompanied by the accumulation of free electrons, which transform the semiconductor into a degenerate semiconductor with metallic characteristics, thus improving the conductivity of materials [28,35,36]. Oxygen vacancies also offer unsaturated coordination sites that alter the electron structure, charge density, and conversion in the p-band center of materials, thus improving its inherent electron transport frequency and catalytic performance [29,37–39]. Despite these benefits, the Schottky barrier forms at the surface/interface of the electrocatalyst and electrode or electrolyte results in the poor conductivity and the low number of active sites of  $WO_3$ , which hinders the catalytic performance [37,40]. Therefore, the composition and structure of tungsten oxide are designed to modify the electronic structure, improve the conductivity, and increase the number of catalytic active sites [36].

Various effective strategies have been developed to optimize nanostructures of tungsten oxide, thus further enhancing its catalytic properties, as shown in Figure 1. (1) Crystal phase regulation: different crystal phases of the samples have different degrees of interatomic *d-sp* orbital hybridization and lattice expansion, thus showing different band gaps and catalytic activities [41–43]. Tungsten oxide exhibits tunable catalytic properties due to its adaptable conversion between stoichiometric and non-stoichiometric crystal phases. (2) Morphology regulation: preparing tungsten oxides with various morphologies to expose different surfaces can optimize their adsorption free energy and intrinsic activity, which is of great significance to improve catalytic performances. Additionally, it is shown that the morphology regulation of tungsten oxide can effectively adjust the band gaps and the number of active sites [44]. (3) Defect engineering, including controlling the lattice vacancy and hetero atom doping, has also been used to enhance the intrinsic catalytic activity of tungsten oxide by effectively regulating the electronic structure and increasing the number of active sites [45–47]. Numerous experimental and theoretical findings have demonstrated that the introduction of defects to construct tungsten oxide with a non-stoichiometric ratio is more conducive to the adsorption/desorption of intermediate molecules ( $*H$  for HER;  $*OH$  and  $*OOH$  for OER) at the oxygen vacancy and doping sites [35,48,49]. (4) Benefiting from the synergistic effect, the construction of a heterostructure with specific interface configurations has been proved to be an effective way of reducing the reaction barrier of water splitting and promoting the adsorption and desorption of protons [36,50–53]. In this case, the highly efficient catalytic electrodes possess high electron transport capacity and large active surface area, which might provide sufficient active sites and appropriate adsorption strength. Numerous heterostructures with stable structures, high specific surface areas, and abundant active sites, including semiconductor- $WO_x$ ,  $WO_x$ -C, and metal- $WO_x$  heterostructures, have been developed [54–57]. These fantastic efforts substantially promoted the development of tungsten oxide-based electrocatalysts.

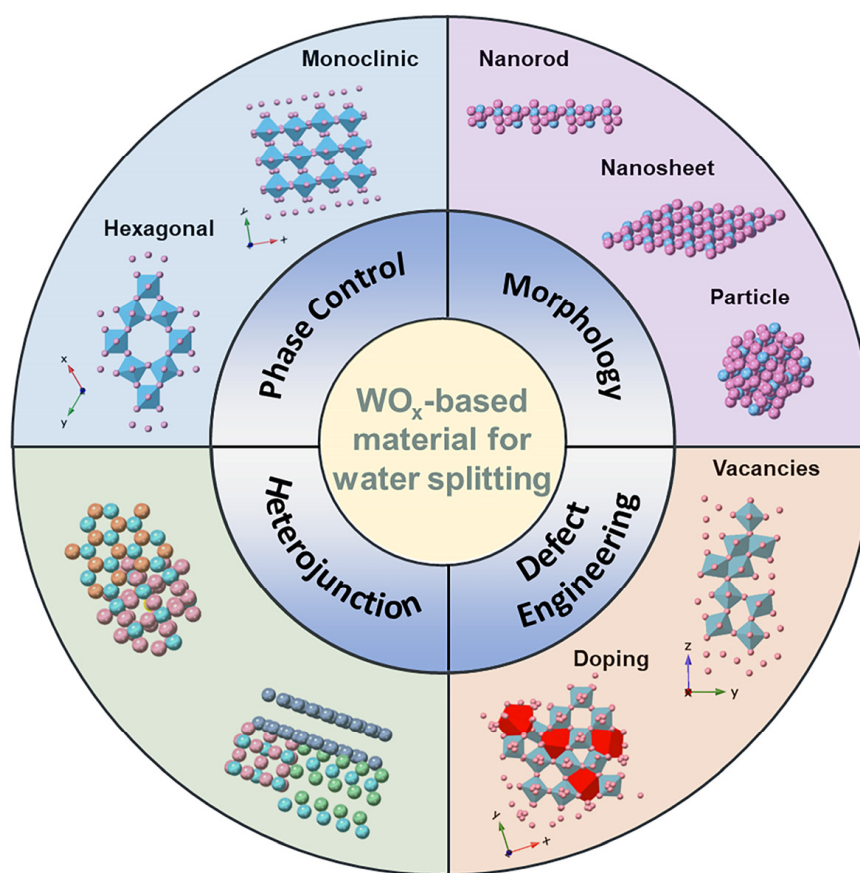


**Figure 1.** Strategies for improving the electrocatalytic performances of  $\text{WO}_x$ -based electrocatalysts.

Tungsten oxides are widely utilized in energy storage [58–63], sensors [64–68], catalysis [69–74], and other fields because of their adjustable valence states ( $\text{W}^{4+}$ ,  $\text{W}^{5+}$ , and  $\text{W}^{6+}$ ) and band gaps [31,75,76], various morphologies from zero to three dimensions [44,77], and different crystal phases. Here, the research progress of tungsten oxide-based electrocatalysts for water splitting over the last few years is reviewed. Emphatically discussed are the impacts of crystal phase, morphology, defect engineering, and heterojunction effects on the electronic structure and catalytic activity of tungsten oxide-based nanomaterials. We also present a brief summary and outlook of the tungsten oxide catalyst research, with the intention that this review may provide some insights into the construction of high-efficiency oxide catalysts.

## 2. Phase Control

Controlling the crystal phase of tungsten oxide and optimizing its physical and chemical properties have been proven effective in improving catalytic performance [41,42]. The  $\text{WO}_x$  is not simply composed of  $\text{W}^{6+}$  and  $\text{O}^{2-}$  ions, which mainly consist of hybrid conduction and valence band states of W 5d and O 2p [32]. The electronic structure of  $\text{WO}_x$  in different crystal phases, such as monoclinic, orthorhombic, and hexagonal phases, is affected by the W–O bond length [32,78,79]. Consequently, it is possible to optimize their catalytic performances by carefully adjusting the crystal phases [30,32,80]. The relatively stable monoclinic and metastable hexagonal phases have attracted extensive research for electrocatalytic performances due to their tunnel structure and rich intercalation [81]. The synthesis methods and the properties (electrolyte, over-potentials at  $10 \text{ mA cm}^{-2}$ , and Tafel slopes) of tungsten oxide-based electrodes with different phases are summarized in Table 1.

**Table 1.** Application of tungsten oxide-based catalyst with different phases in water splitting.

Electrocatalyst	Synthesis Method	Electrolyte	Application	Scanning Speed (mV s <sup>-1</sup> )	Overpotential at 10 mA cm <sup>-2</sup> (mV)	Tafel Slope (mV dec <sup>-1</sup> )	Ref.
Monoclinic WO <sub>3</sub> ·2H <sub>2</sub> O	Wet-chemical route	0.5 M H <sub>2</sub> SO <sub>4</sub>	HER	5	117	66.5	[40]
Orthorhombic WO <sub>3</sub> ·H <sub>2</sub> O					209	198	
Orthorhombic WO <sub>3</sub> ·0.33H <sub>2</sub> O					276	376.5	
Hexagonal-WO <sub>3</sub>	Hydrothermal method	0.5 M H <sub>2</sub> SO <sub>4</sub>	HER	2	83	48	[42]
Monoclinic-WO <sub>3</sub>					106	78	
m-WO <sub>3</sub>	Hydrothermal method, thermal treatment	0.5 M H <sub>2</sub> SO <sub>4</sub>	HER	5	168	83	[41]
h-WO <sub>3</sub>					257	157	
Monoclinic WO <sub>3</sub>	In ethanol and kept under ambient temperature, thermal treatment	0.5 M H <sub>2</sub> SO <sub>4</sub>	HER	1	73	39.5	[82]
Orthorhombic WO <sub>3</sub> ·H <sub>2</sub> O					147	43.9	

Heat treatment is an effective way to control the crystal phase of WO<sub>x</sub>-based nanomaterials, in which the temperature is a vital factor. For instance, Guninel et al. annealed orthotropic WO<sub>3</sub>·H<sub>2</sub>O in air, and they found that the crystal structure transformed to monoclinic WO<sub>3</sub> with the disappearance of water molecules in the structure. The detailed dehydration process is shown in Figure 2a [83]. Pradhan et al. also have prepared the monoclinic WO<sub>3</sub> by annealing orthotropic tungsten oxide hydrate at 400 °C in the air (Figure 2b) [82]. It shows that the double-layer capacitance (C<sub>dl</sub>) of monocline WO<sub>3</sub> is 2.83 times that of the original WO<sub>3</sub>·H<sub>2</sub>O, providing more active surfaces during the catalytic reaction. As a result, the monoclinic WO<sub>3</sub> exhibits an over-potential of 73 mV at 10 mA cm<sup>-2</sup> in 0.5 M H<sub>2</sub>SO<sub>4</sub>, which is much lower than that of orthorhombic tungsten oxide hydrate (147 mV). The density functional theory (DFT) results (Figure 2c) proved that the hydrogen proton adsorption energy on P2 1/n monocline WO<sub>3</sub> (200) is more suitable than that of Pt (111). Halder's group investigated the effect of heat treatment temperatures on the phase transition. With the increase in calcination temperature, the crystal phase of WO<sub>3</sub> changed from hexagonal to monoclinic and then to cubic phase [84]. The phase transformation process from hexagonal to monoclinic at 550 °C was further observed by in situ transmission electron microscopy (TEM). The monoclinic WO<sub>3-x</sub> obtained at this temperature exhibits the best HER activity because of the highest oxygen vacancy concentration.

Certain additives also have an impact on the crystal phase of tungsten oxide during the preparation process. Song's team precisely prepared the orthorhombic WO<sub>3</sub>·0.33H<sub>2</sub>O and monoclinic WO<sub>3</sub>·2H<sub>2</sub>O by utilizing ethylene diamine tetra acetic acid and DL-malic acid at room temperature, respectively (Figure 2d) [40]. It demonstrated that a lower over-potential (117 mV) and Tafel slope (66.5 mV dec<sup>-1</sup>) of monoclinic WO<sub>3</sub>·2H<sub>2</sub>O were required to reach a current density of 10 mA cm<sup>-2</sup> in 0.5 M H<sub>2</sub>SO<sub>4</sub> (Figure 2e).

Hajiahmadi et al. explored the reaction mechanism and adsorption model of hex-WO<sub>3</sub> (001) in acid oxygen evolution reaction (OER) (Figure 3) [85]. There are six adsorption models involved: (1) Initial state. The H<sub>2</sub>O adsorbs at the top of the central W site due to the lack of coordination of the central tungsten. (2) Water decomposes to form OH\* and H<sup>+</sup>, which are the most stable configurations co-adsorbed at the top W site and adjacent O site, respectively. (3) Dehydrogenation of OH\* to form O\*. The dissociated hydrogen is adsorbed to another nearby oxygen. (4) The adsorption of water molecule on O\*. (5) Dehydrogenation of O\*·H<sub>2</sub>O to form OOH\*. (6) Dehydrogenation of OOH\* to form O<sub>2</sub>.

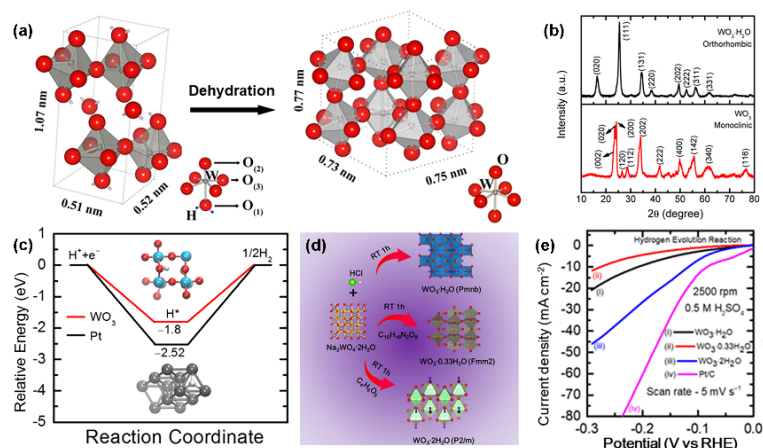


**Figure 2.** (a) Schematic of the orthorhombic unit cell of tungstite, which converts to the monoclinic tungsten oxide unit cell by dehydration at elevated temperatures ( $\geq 300$  °C). Reprinted with permission from [83], with permission from Springer, 2014. (b) XRD patterns of orthorhombic  $\text{WO}_3 \cdot \text{H}_2\text{O}$  and monoclinic  $\text{WO}_3$ . (c) Calculated energy landscapes of the HER on  $\text{WO}_3$  (200) and Pt (111). Reprinted with permission from [82], with permission from American Chemical Society, 2017. (d) Synthesis process and (e) linear sweep voltammograms at 2500 of hydrated tungsten oxide ( $\text{WO}_3 \cdot n\text{H}_2\text{O}$ ,  $n$  values 0.33, 1.00, or 2.00) at room temperature. Reprinted with permission from [40], with permission from American Chemical Society, 2020.

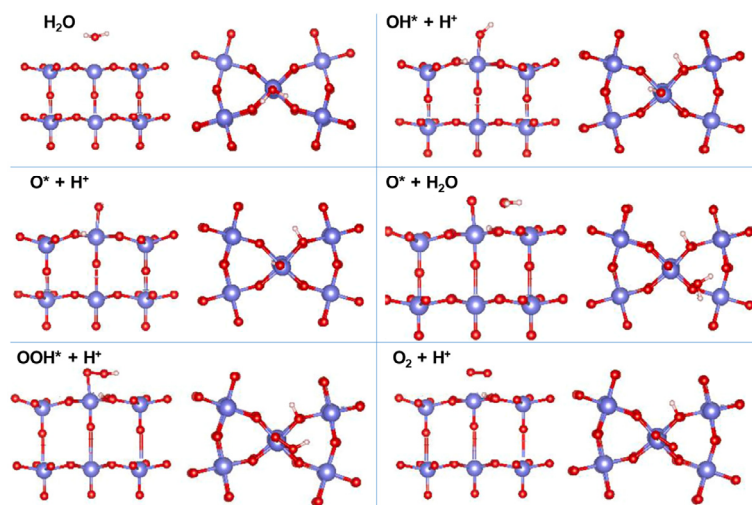


**Figure 3.** Optimized geometries of hex- $\text{WO}_3$  at each step in the acid oxygen evolution reaction, top and side view. O: red, W: purple, H: white. Reprinted with permission from [85], with permission from Elsevier, 2022.

### 3. Morphology Control

Due to their flexible crystal structures,  $\text{WO}_x$  nanomaterials with rich morphologies exhibit different physical and chemical properties. Reasonable design of catalyst morphology may increase the contact area between catalyst and electrolyte, thus improving the electrocatalytic performance. The impact of morphology on the catalytic performance of  $\text{WO}_x$  has been studied recently, and some advancements have been made [42,86,87].

One-dimensional nanostructures, such as nanorods [38] and nanowires [88–90], have been extensively studied in tungsten oxide-based nanomaterials. For example, Liang’s group prepared  $\text{WO}_3$  nanowires with rich oxygen vacancy ( $\text{WO}_3\text{-V}_\text{O}$  NWs) by hydrothermal method combined with plasma sputtering [89]. The  $\text{WO}_3\text{-V}_\text{O}$  NWs grew along the [001] direction ( $c$  axis) and exhibited stable electrocatalytic oxygen evolution activity under acidic conditions. Two-dimensional nanostructures have also attracted extensive attention due

to their increased surface area, abundant active sites, and appropriate adsorption of intermediates in recent years. Pradhan et al. prepared tungsten oxide hydrate nanoplates with apparent gaps between the stacked nanoplates using the hydrothermal method [82]. Guo's group prepared hierarchical  $\text{WO}_3$  nanowire arrays on nanosheet arrays ( $\text{WO}_3$  NWA-NSAs) by the hydrothermal method for alkaline OER [29]. The  $\text{WO}_3$  NWA-NSAs electrocatalyst only requires an over-potential of 230 mV to reach the current density of  $10 \text{ mA cm}^{-2}$  because of its unique hierarchical structure. By changing the composition of surfactants and synthesis parameters of hydrothermal processes, Rajalakshmi et al. prepared various  $\text{WO}_3$  nanomaterials, including one-dimensional nanowires and nanorods, two-dimensional nanoflakes and nanobelts, and three-dimensional nanoparticles, which are star-like and globule-like structures (Figure 4a–g). The influence of morphology on the band gap width and hydrogen evolution performance was also investigated [44]. It was found that the band gaps of tungsten oxide with different morphologies are inconsistent. Among them,  $\text{WO}_3$  nanorods have a higher aspect ratio and better bandgap and adsorption energy in conjunction with the precise cutting of crystal facets along the (001) direction. As a result, the HER performance of one-dimensional  $\text{WO}_3$  nanorods exceeds other morphologies in an acidic electrolyte. For the three-dimensional nanostructure, our group investigated the effect of the etching agent concentration on the morphologies and the alkaline OER performances of Ni- $\text{WO}_3$  nanostructures [91]. The Ni- $\text{WO}_3$  octahedral structure (Figure 4h) was in situ etched with  $(\text{NH}_4)_2\text{SO}_4$ , and the serrated Ni- $\text{WO}_3$  (Figure 4i) was obtained. It was found that the crystal phase of Ni- $\text{WO}_3$  was unaffected by the concentration of the etching agent, but the serrated Ni- $\text{WO}_3$  dramatically improves OER performance (an over-potential of only 265 mV at  $10 \text{ mA cm}^{-2}$ ) compared with octahedral Ni- $\text{WO}_3$  (365 mV).

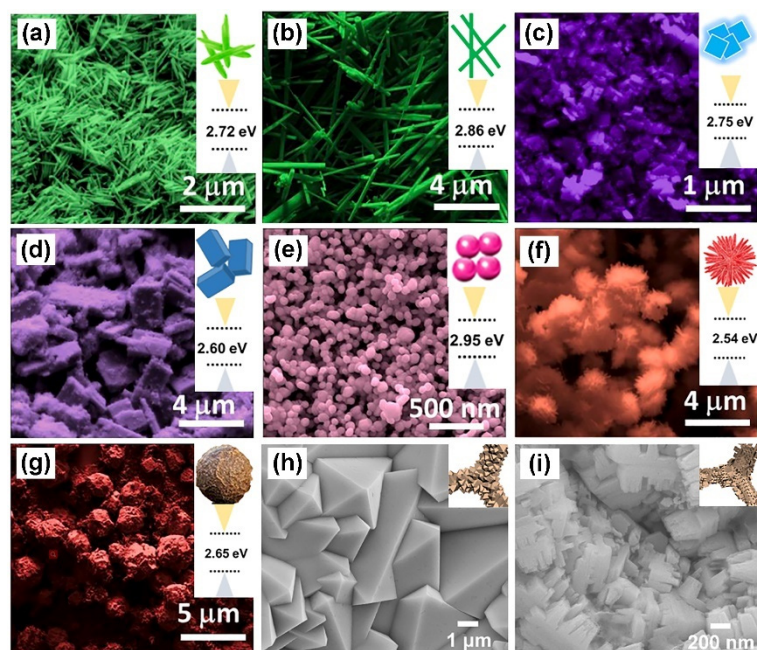


**Figure 4.** FESEM image and of bandgap (a)  $\text{WO}_3$  nanowires (W-NW), (b)  $\text{WO}_3$  nanorods (W-NR), (c)  $\text{WO}_3$  nanoflakes (W-NF), (d)  $\text{WO}_3$  nanobelts (W-NB), (e)  $\text{WO}_3$  nanoparticles (W-NP) of W-NP, (f)  $\text{WO}_3$  star-like structures (W-S), and (g)  $\text{WO}_3$  globule-like structures (W-G). Reprinted with permission from [44], with permission from Elsevier, 2022. FESEM image of octahedron-like (h,i) serrated Ni- $\text{WO}_3$ . Reprinted with permission from [91], with permission from Elsevier, 2022.

#### 4. Defect Engineering

Defect engineering, including oxygen vacancy construction and hetero atom doping, reduces the atomic coordination numbers in the material and, thus, regulates the electronic structure [89,92]. The band gap and the adsorption-free energy of the catalyst could be optimized by regulating the electronic structure of the catalyst, thus reducing the catalytic

reaction barrier and improving the reaction kinetics. These doping and defect sites can also potentially increase the number of active sites and the concentration of free carriers, which are essential for reducing the reaction barrier and increasing the electron transfer efficiency [93]. The synthesis methods and the properties (electrolyte, over-potentials at  $10 \text{ mA cm}^{-2}$ , and Tafel slopes) of tungsten oxide-based electrodes modified by defect engineering are summarized in Table 2.

**Table 2.** Application of tungsten oxide-based catalyst modified by defect engineering in water splitting.

Electrocatalyst	Synthesis Method	Electrolyte	Application	Scanning Speed ( $\text{mV s}^{-1}$ )	Overpotential at $10 \text{ mA cm}^{-2}$ (mV)	Tafel Slope ( $\text{mV dec}^{-1}$ )	Ref.
$\text{WO}_{3-r}$	Liquid exfoliation	0.5 M $\text{H}_2\text{SO}_4$	HER	2	38	38	[94]
$\text{WO}_{3-x}$	Electrospinning	0.5 M $\text{H}_2\text{SO}_4$	HER	5	185	89	[95]
Meso- $\text{WO}_{2.83}$	$\text{H}_2$ reduction	0.5 M $\text{H}_2\text{SO}_4$	HER	5	287	95	[35]
$\text{WO}_{2.9}$	Wet grinding method, thermally treated	0.5 M $\text{H}_2\text{SO}_4$	HER	5	70	50	[96]
Oxygen vacancies-rich tungsten oxides	Hydrothermal method, thermal treatment	1 M KOH	HER	5	25	49.25	[97]
$\text{W}_{18}\text{O}_{49}$	Microwave-solvothermal treatment	0.5 M $\text{H}_2\text{SO}_4$ 0.1 M $\text{Na}_2\text{SO}_4$	HER	5	54 ~200	30 80	[98]
Ta-doped $\text{WO}_3$	Hydrothermal method	1 M $\text{H}_2\text{SO}_4$	HER	2	480	65	[99]
Ir-doped $\text{WO}_3$	Hydrothermal method, thermal treatment	0.5 M $\text{H}_2\text{SO}_4$	OER	1	258	48.9	[100]
			HER		36	92	
			OWS		1.56	-	
W/ $\text{WO}_2$	Hydrothermal method, thermal treatment	0.5 M $\text{H}_2\text{SO}_4$	HER	5	297	74.5	[101]
4% Sm doped $\text{WO}_3$	Hydrothermal method	0.5 M $\text{H}_2\text{SO}_4$	HER	5	54	74.5	[102]
5% Sm doped $\text{WO}_3$			OER		90	138	
4% Sm doped $\text{WO}_3$   15% Sm doped $\text{WO}_3$			OWS		1.6 V	-	
Ag- $\text{WO}_3$	Sonochemical method	0.5 M $\text{H}_2\text{SO}_4$	HER	2	207	52.4	[103]
Pt-SA/ML- $\text{WO}_3$	Space confined strategy, thermal treatment	0.5 M $\text{H}_2\text{SO}_4$	HER	2	22	27	[104]
Ni- $\text{WO}_2$ /CP	Hydrothermal method, thermal treatment	1 M KOH	HER	5	83	79	[105]
Ni- $\text{WO}_2$ /NF					41	47	
Fe-P/ $\text{WO}_2$	Organic-inorganic hybridization method	0.5 M $\text{H}_2\text{SO}_4$	HER	5	48	47	[106]
$\text{Ni}_{0.19}\text{WO}_4$	Hydrothermal method, thermal treatment	1 M KOH	OER	5	240	47	[107]
			HER		200	78	
			OWS		1.59 V	-	
Co- $\text{WO}_{2.7-x}$	Hydrothermal method, thermal treatment	1 M KOH	HER	5	59	86	[48]
Ni/ $\text{WO}_x$	Hydrothermal method, thermal treatment	1 M KOH	HER	5	42	57.9	[108]
			OER		395.7@100 $\text{mA cm}^{-2}$	100	
			OWS		1.52	-	

Table 2. Cont.

Electrocatalyst	Synthesis Method	Electrolyte	Application	Scanning Speed (mV s <sup>-1</sup> )	Overpotential at 10 mA cm <sup>-2</sup> (mV)	Tafel Slope (mV dec <sup>-1</sup> )	Ref.
Ni-doped W <sub>18</sub> O <sub>49</sub>	Hydrothermal method, thermal treatment	1 M KOH	HER	2	90	92	[93]
			OER		240@20 mA cm <sup>-2</sup>	106	
			OVS		1.56 V	-	
10 wt% Ir/W <sub>18</sub> O <sub>49</sub> nanowire	Solvothetmalsonication and dispersion, thermal treatment	0.5 M H <sub>2</sub> SO <sub>4</sub>	HER	5	41	38	[109]
		1 M PBS			83	66	
Fe-WO <sub>x</sub>	Hydrothermal	1 M KOH	OER	-	380	51.7	[110]
Ni <sub>0.78</sub> WO <sub>2.72</sub>	Wet chemical, thermal treatment	0.1 M KOH	OER	10	270	-	[111]
Pt SA/WO <sub>3-x</sub>	Incipient wetness impregnation method	0.5 M H <sub>2</sub> SO <sub>4</sub>	HER	5	47	45	[112]
Ru-WO <sub>2.72</sub>	Hydrothermal method, self reduction	0.5 M H <sub>2</sub> SO <sub>4</sub>	HER	5	40	50	[113]
Ag/WO <sub>3-x</sub>	Situ reduction method	0.5 M H <sub>2</sub> SO <sub>4</sub>	HER	5	30	40	[114]
Mo-W <sub>18</sub> O <sub>49</sub>	Hydrothermal method	0.5 M H <sub>2</sub> SO <sub>4</sub>	HER	5	45	54	[115]
NiFe-W <sub>18</sub> O <sub>49</sub>	Hydrothermal method	0.1 M KOH	OER	5	325	42	[116]
5 at% Pd doped W <sub>18</sub> O <sub>49</sub>	Solvothetmal method	0.5 M H <sub>2</sub> SO <sub>4</sub>	HER	1	137	35	[117]
1 at% Mo incorporated W <sub>18</sub> O <sub>49</sub> nanofibers	Solvothetmal method	0.5 M H <sub>2</sub> SO <sub>4</sub>	HER	1	262	49	[118]
Co <sub>0.5</sub> Fe <sub>0.5</sub> WO <sub>4</sub>	A polyol route	1 M KOH	OER	1	360	36.3	[119]
Pt/def-WO <sub>3</sub>	Hydrothermal method and deposition-precipitation method	0.5 M H <sub>2</sub> SO <sub>4</sub>	HER	1	42	61	[120]

#### 4.1. Oxygen Vacancy

Tungsten oxide-based nanomaterials with abundant oxygen defects show great potential for water splitting. Abundant oxygen vacancies can improve the conductivity and promote the adsorption of OH<sup>-</sup>, thus effectively increasing the oxygen evolution activity [89]. For example, Guo's research group prepared WO<sub>3</sub> with rich oxygen vacancies by hydrothermal method, and they explored its oxygen evolution properties in the alkaline electrolyte [29]. The abundant oxygen vacancy not only improves the conductivity of WO<sub>3</sub>, but also modifies its electronic structure, so that WO<sub>3</sub> only needs 230 mV overpotential to reach the current density of 10 mA cm<sup>-2</sup>.

Effect of oxygen vacancy on morphology and properties of WO<sub>x</sub>. Two extra electrons are produced when an O atom is removed from the WO<sub>3</sub> structure. One or two electrons can be transferred to a neighboring W atom to form the W<sup>5+</sup> or W<sup>5+·</sup>-W<sup>5+</sup> centers [32]. Additionally, introducing the O-vacancy modifies the splitting of the W-O bond, increases the W-W distance at the O-vacancy position, and narrows the WO<sub>3</sub> band gap accordingly (Figure 5a–d) [79]. The electrode's conductivity is improved as a result of abundant oxygen vacancies, which can turn an n-type WO<sub>x</sub> semiconductor into a degenerate semiconductor with metallic characteristics (Figure 5e) [35,89]. Besides, a high oxygen vacancy concentration will increase the material's surface roughness and the area in contact with the electrolyte. For example, the surface of tungsten oxide with a smooth hexahedral structure (Figure 5f) turns rough after being annealed in a H<sub>2</sub> atmosphere, forming a porous structure (Figure 5g) [121]. As shown in Figure 5h,i, the porous WO<sub>2</sub> HN/NF has a BET surface area, pore size, and specific volume of 22.8 m<sup>2</sup> g<sup>-1</sup>, 10–100 nm, and 0.138 cm<sup>3</sup> g<sup>-1</sup>, respectively. Owing to the highly concentrated oxygen vacancies that provide more active

sites and narrower band gaps, the porous WO<sub>2</sub> HN/NF electrode showed lower potential and excellent catalytic stability in HER, OER, and overall water splitting.

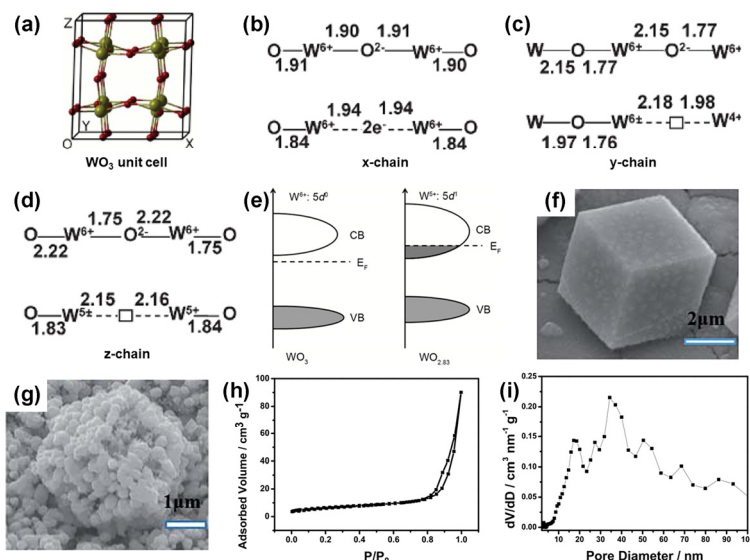


**Figure 5.** (a) Ball-and-stick model of RT monoclinic WO<sub>3</sub> unit cell with 32-atom or 64-atom. The large green (gray) and small red (dark) balls represent the W and O atoms, respectively. The *x* (b), *y* (c), and *z* (d) direction -W-O-W- chains with (WO<sub>3-x</sub>, *x* = 0.12 for 32-atom, *x* = 0.06 for 64-atom) and without (WO<sub>3</sub>) oxygen vacancy. Distances are in Å. The two excess electrons are created by removing a neutral O atom from WO<sub>3</sub>, which can be either paired up in a singlet (closed shell) spin state or unpaired in a triplet spin state. Reprinted with permission from [79], with permission from the American Physical Society, 2011. (e) Schematic illustration of the band structures of Meso-WO<sub>2.83</sub> and Meso-WO<sub>3</sub>. Reprinted with permission from [35], with permission from the Royal Society of Chemistry, 2018. SEM of the WO<sub>2</sub> hexahedral networks supported on nickel foam before (f) and after (g) calcination. (h) N<sub>2</sub> adsorption-desorption isotherms of porous WO<sub>2</sub> HN/NF and (i) corresponding pore size distribution. Reprinted with permission from [121], with permission from the Royal Society of Chemistry, 2017.

Oxygen vacancy recognition. First, the O vacancy can be directly observed by atomic high-resolution TEM (HRTEM), where the variation in atomic column intensity indicates the variation in oxygen atomic occupation. As shown in Figure 6a, the tiny pits shown by the arrows indicate the presence of oxygen vacancies [89]. The variations in intensity and contrast were further highlighted in the colored image and the line profile (Figure 6b). Second, UV-vis diffuse reflectance spectroscopy and UV-vis absorption spectroscopy are also used to identify oxygen vacancy defects. As shown in Figure 6c,d, a stronger photoresponse in the visible to infrared region indicates a higher O vacancy concentration in the material [35,40,122]. Besides, electron paramagnetic resonance (EPR), a technique for detecting the chemical environment of unpaired electrons in atoms or molecules, can be used to confirm the existence of oxygen vacancies (Figure 6e). When oxygen vacancies capture electrons, symmetrical EPR signals appear at the position  $g \approx 2.002$ . The stronger the intensity of the EPR signal, the higher concentration of oxygen vacancies present in the material [35,89]. Notice that the oxygen vacancy also changes the metal valence in the metal oxide. Therefore, in addition to the direct characterization methods of oxygen vacancies, alternative techniques, such as X-ray photoemission spectroscopy (XPS) and synchrotron X-ray absorption fine structure (XAFS), can also be employed to infer the existence of oxygen vacancies. As shown in Figure 6f, after the oxygen vacancy was introduced, the XPS peaks of W 4f were moved to the lower binding energy region [35,38,122]. For O1s XPS, the peak at ~531.3 eV corresponds to the oxygen vacancy [35,123–125].

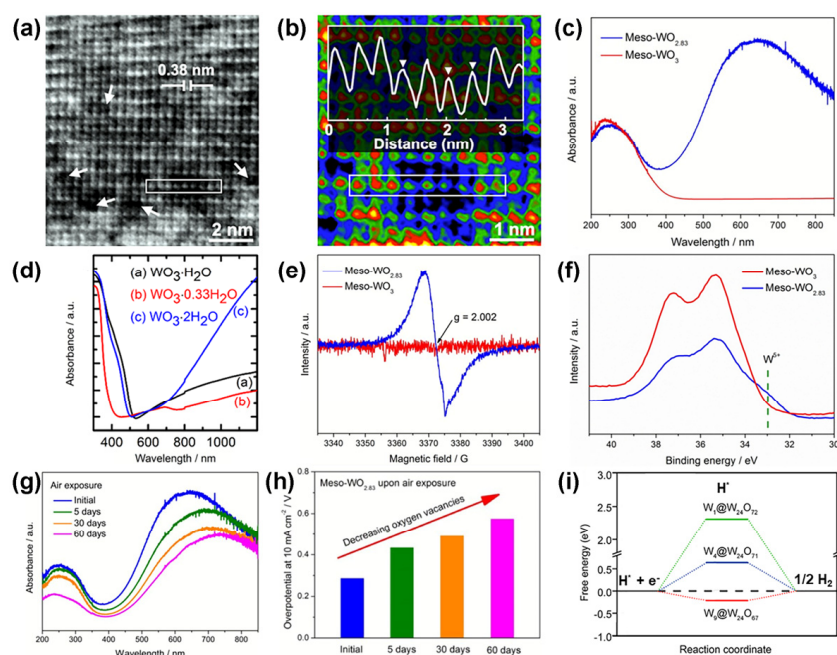


**Figure 6.** (a) TEM images (Numerous small pits shown by the arrows provide more coordinated unsaturated sites for OER electrocatalysis) and (b) colored atomic-resolution TEM image of  $\text{WO}_3\text{-V}_\text{o}$  with a line profile of nine atoms (indicated by a box), the differences in intensity and contrast are further highlighted in the colored image and the line profile. Reprinted with permission from [89], with permission from the Chinese Chemical Society, 2020. (c) UV/vis diffuse reflectance spectra of Meso- $\text{WO}_3$  and Meso- $\text{WO}_{2.83}$ . Reprinted with permission from [35], with permission from the Royal Society of Chemistry, 2018. (d) UV-vis absorption spectra of  $\text{WO}_3\cdot\text{H}_2\text{O}$ ,  $\text{WO}_3\cdot 0.33\text{H}_2\text{O}$ , and  $\text{WO}_3\cdot 2\text{H}_2\text{O}$ . Reprinted with permission from [40], with permission from the American Chemical Society, 2020. (e) EPR spectra at room and (f) XPS of Meso- $\text{WO}_3$  and Meso- $\text{WO}_{2.83}$ . (g) UV/vis diffuse reflectance spectra and (h) the overpotential comparison at the current density of  $10 \text{ mA cm}^{-2}$  of the Meso- $\text{WO}_{2.83}$  products upon air exposure time. Reprinted with permission from [35], with permission from the Royal Society of Chemistry, 2018. (i) Free-energy diagram for hydrogen adsorption at the W site on the  $\text{WO}_3$  (010) slab with different O vacancies. Reprinted with permission from [94], with permission from the American Chemical Society, 2017.

**Effect of oxygen vacancy concentration on performance.** To further investigate the impact of oxygen vacancy concentration on catalytic performance, Thomas et al. explored the relationship between the electrocatalytic performance of Meso- $\text{WO}_{2.83}$  and surface oxidation degree brought on by exposure to air (Figure 6g,h) [35]. With the increase in exposure time, the plasmon resonance of Meso- $\text{WO}_{2.83}$  was weakened, accompanied by a red shift, and its electrocatalytic activity gradually decreased, as well. This indicates that abundant oxygen vacancies are advantageous for enhancing catalytic activity. Zeng et al. demonstrated that abundant oxygen vacancies could optimize the hydrogen adsorption Gibbs free energy ( $\Delta G_{\text{H}^*}$ ) using the DFT (Figure 6i) [94].

**Method of producing oxygen vacancy.** Oxygen vacancies are widespread in transition metal oxides because of their low formation energy [35,39]. Representative methods of producing oxygen vacancies in metal oxides include heat treatment, reductive treatments, and other methods [38,126]. The first method is heat treatment, which involves removing a small amount of lattice oxygen from metal oxides in low-oxygen conditions at high temperatures without causing bulk phase transition. The oxygen vacancy concentration can be adjusted by controlling the heat treatment temperature or the inert gas flow rate. For instance, Halder's group thermally treated  $\text{WO}_3$  in a vacuum environment to produce  $\text{WO}_{3-x}$  with rich oxygen vacancies [84]. The second method of producing oxygen vacancies in tungsten oxide is reductive treatments, which create oxygen vacancies with the aid of

reducing agents, such as  $H_2$  [123],  $NaBH_4$  [127,128], and sodium dodecyl sulfate [29]). Taking the reduction in hydrogen as an example, with the extension of reduction time,  $WO_3$  gradually evolved into  $WO_{3-x}$ ,  $WO_2$ , and finally, metallic  $W^0$  [129]. Thomas et al. prepared Meso- $WO_{2.83}$  with oxygen-rich vacancies by replacing bulk materials with mesoporous materials to increase the reduction rate in the hydrogen atmosphere [35]. Due to the slow diffusion of  $H_2$  molecules in bulk materials, the use of mesoporous  $WO_3$  with a higher surface area and thin nanoscale pore wall allows  $H_2$  molecules to diffuse and migrate more easily on its surface and inside. The results show that the mesoporous structure not only dramatically reduces the  $H_2$  reduction temperature, but also selectively generates  $WO_{2.83}$ . Other methods of producing oxygen vacancies include plasma treatment, flame, mechanical exfoliation, and hydrothermal methods [29,89,130,131]. For example, as a surface treatment technology, plasma has a certain reduction ability, and the oxygen vacancy generated by it only exists on the surface of the sample [131].

#### 4.2. Hetero Atom Doping

Hetero atom doping is also an effective strategy to prepare tungsten oxide-based nanomaterials with abundant defects, which achieve a significant leap in catalytic performance by regulating the electronic coordination environment, the number of active sites, and the adsorption strength of intermediates [48,113]. In practical applications, atom-doped materials usually contain both hetero atoms and oxygen vacancies, which can cooperatively promote the catalytic activity [93,118,132]. The effect of doping on catalytic performance can be adjusted by changing the type [48,105] and concentration [115,118,133] of hetero atoms. Atom doping could be divided into noble metal atomic doping and non-noble metal atomic doping. For the former, the noble metal atoms typically exist as single atoms or atomic clusters to reduce the costs and improve the utilization rate of noble metal atoms [112,113,134–136]. For example, Hou et al. reported Pt sing-atoms supported on monolayer  $WO_3$  (Pt-SA/ML- $WO_3$ ) for HER [104]. The high-angle annular dark-field scanning transmission electron microscopy (HAADF-STEM) images (Figure 7a,b) and ICP result showed that 0.20 wt% Pt atoms were immobilized on ML- $WO_3$ . HRTEM images demonstrate the existence of defects, including lattice distortion, as well as W and O vacancies (Figure 7c,d). The HER performance of Pt-SA/ML- $WO_3$  (over-potential of 22 mV at  $10\text{ mA cm}^{-2}$ , Tafel slope of  $27\text{ mV dec}^{-1}$ ) was even better than that of 20% Pt/C (over-potential of 34 mV at  $10\text{ mA cm}^{-2}$ , Tafel slope of  $28\text{ mV dec}^{-1}$ ). The improved performance is mainly attributed to the strong interaction between Pt single atoms and ML- $WO_3$ , which drastically tunes the electronic structure of the catalyst, endowing Pt-SA/ML- $WO_3$  with a strong conductivity and an adequate  $\Delta G_{H^*}$  (Figure 7e). Sun et al. investigated the overall water-splitting performance of the iridium-doped tungsten trioxide array (Ir-doped  $WO_3$ ) in acidic conditions [100]. Ir can preempt some of the electrons in the  $WO_3$  matrix to optimize its electronic structure because  $Ir^{4+}$  has a smaller radius and a higher atomic number than  $W^{6+}$ . The Ir-doped  $WO_3$  exhibited low cell voltages of 1.56 and 1.68 V to drive the current densities of 10 and  $100\text{ mA cm}^{-2}$ , respectively. Ma's group analyzed the effects of oxygen vacancy and Ru doping on electronic states and  $d$ -band center of  $WO_3$  by density functional theory (DFT) calculations [136]. As shown in Figure 7f, when only oxygen vacancies exist, the electrons produced by oxygen vacancies are transferred to neighboring W atoms. After doping Ru atom, electrons are mainly transferred from Vo site to adjacent Ru site, and a few electrons are transferred to an adjacent W site. Therefore, Ru sites with sufficient electrons in Vo- $WO_3$ /Ru SAs may be active centers for adsorption intermediates in acidic media. In alkaline and neutral solutions, the oxygen atoms in water molecules are more easily captured by the electron-deficient W site, and the generated  $H^*$  migrates to the nearby Ru site to form  $H_2$ . In addition, the  $d$ -band center of Vo- $WO_3$ /Ru SAs ( $-5.180\text{ eV}$ ) is much lower than that of  $WO_3$  ( $-3.252\text{ eV}$ ) and Vo- $WO_3$  ( $-4.133\text{ eV}$ ), indicating that the strength of  $H^*$  bond is weakened (Figure 7g), which is conducive to the desorption of  $H^*$  from the surface and the promotion of HER.

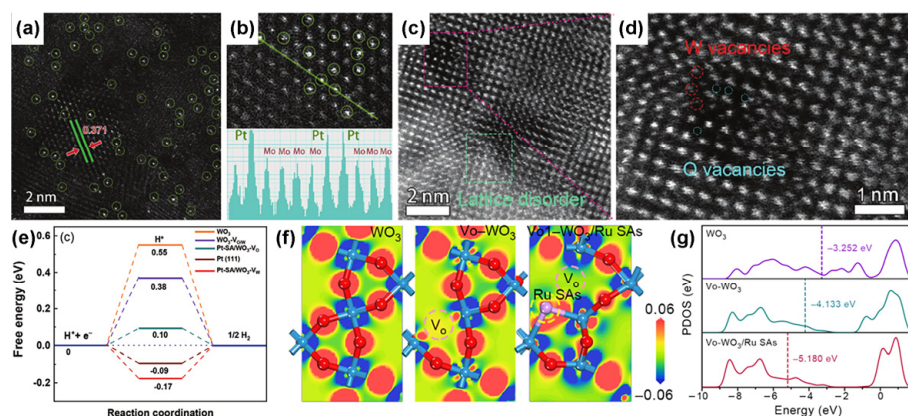


**Figure 7.** (a) HAADF-STEM image, (b) magnified HADDF-STEM image and corresponding intensity profiles of the line section, and (c,d) magnified HADDF-STEM images of Pt-SA/ML-WO<sub>3</sub>. (e) Calculated free energy profiles of HER at the equilibrium potential for WO<sub>3</sub>, WO<sub>3</sub>-V<sub>O/W</sub>, Pt-SA/WO<sub>3</sub>-V<sub>O</sub>, Pt-SA/WO<sub>3</sub>-V<sub>W</sub>, and metal Pt (111). Reprinted with permission from [104], with permission from Wiley, 2021. (f) Electron density difference isosurfaces (where red and blue areas indicate the charge accumulation and depletion, respectively) and (g) partial electronic density of states of WO<sub>3</sub>, Vo-WO<sub>3</sub>, and Vo-WO<sub>3</sub>/Ru SAs. Reprinted with permission from [136], with permission from Elsevier, 2022.

In addition to doping the noble metal atoms, doping of non-noble metal atoms (Co, Fe, Ni, F, and Mo) could also regulate the physicochemical properties of the catalyst and effectively improve the catalytic performance of tungsten oxide-based nanomaterials [48,107,111,115,116,133,137,138]. For example, Xiao et al. simulated the *d*-orbital hybridization of WO<sub>2</sub> by a series of transition metal heteroatoms using first principles and explored HER properties of M-WO<sub>2</sub> (M = Fe, Co, Ni, and Cu atoms) [105]. The Fe, Co, Ni, or Cu heteroatoms replace one of the W atoms (W-M bond) to form higher *d*-band packed atomic coordination, resulting in increased filling of W-M bond antibonding orbitals and weakening of bond strength (Figure 8a). The DFT result showed that the Ni-W site has modest hydrogen adsorption ( $\Delta G_{H^*} = -0.43$  eV) due to the dynamic transfer of some bonded electrons from the W-W/Ni bonds to the Ni-O bonds after the substitution of W atoms by Ni, which reduces the free energy, weakens the metal-metal bond, and increases the bond length of W-W/Ni (Figure 8b). Therefore, Ni-WO<sub>2</sub> only needs 83 mV to reach the current density of 10 mA cm<sup>-2</sup> in an alkaline environment. To investigate the effect of Ni atom doping on the localized structure of tungsten oxide, the author compared the W L<sub>3</sub>-side X-ray absorption near side structures (XANES) and further proved that the addition of Ni atoms can effectively reduce the *d*-band occupation state on W atoms. Comparing the whole contour plots of wavelet transform (WT) (Figure 8c,d) and the charge density difference slices (Figure 8e,f) of WO<sub>2</sub> and Ni-WO<sub>2</sub>, it was found that the R-value at about  $k = 12.2 \text{ \AA}^{-1}$  in the WT spectrum of Ni-WO<sub>2</sub> is increased, and the charge density between Ni-W is significantly decreased. All these results indicate that Ni doping can effectively regulate the coordination strength between metal atoms and reduce the ability to capture electrons of W atoms, which is closely related to the absorption/desorption behavior on the catalyst surface.

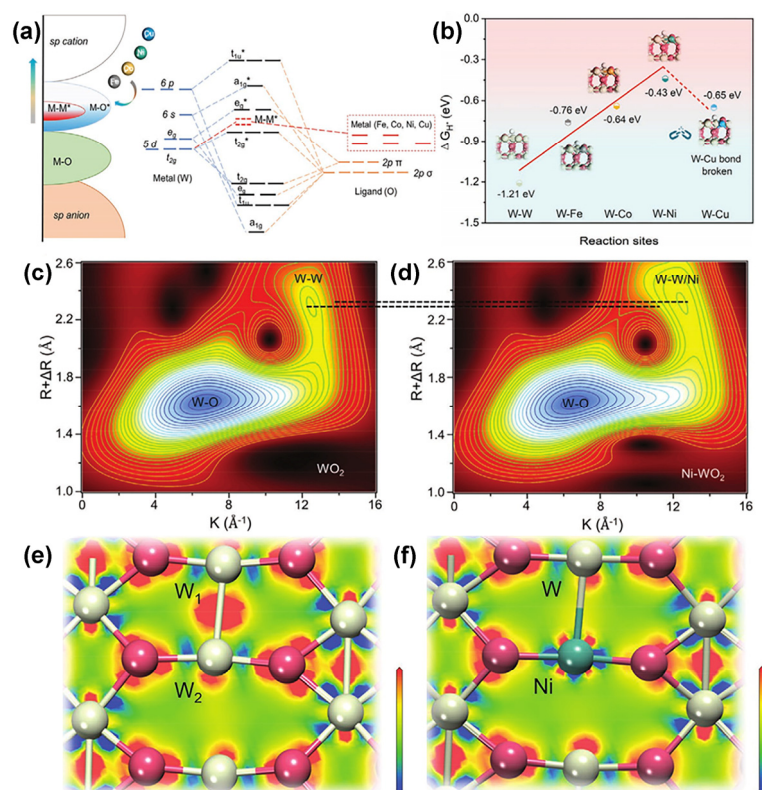


**Figure 8.** (a) Schematic illustration of the W 5d-M 3d orbital modulation of M-WO<sub>2</sub> (M = Fe, Co, Ni, Cu, etc.). (b) The calculated hydrogen adsorption Gibbs free energy on different reaction sites of M-WO<sub>2</sub> (011). The whole contour plots of wavelet transform (WT) of (c) WO<sub>2</sub> and (d) Ni-WO<sub>2</sub>. The top-view electron density difference of (e) WO<sub>2</sub> (011) and (f) Ni-WO<sub>2</sub> (011), ranging from  $-0.1$  to  $0.1 \text{ e } \text{Å}^{-3}$ . Reprinted with permission from [105], with permission from Wiley, 2022.

## 5. Heterostructure Construction

Constructing heterostructured nanomaterials composed of tungsten oxide and another material is an effective strategy to improve the catalytic performance of tungsten oxide [139–141]. The heterostructured nanomaterials reaches the catalytic performance of  $1 + 1 > 2$  by exposing more active sites and promoting interfacial electron transfer, which is called the “spillover” mechanism of the system [52,141]. The synthesis methods and the catalytic properties of tungsten oxide-based heterostructure electrodes with different morphologies (such as nanowires, nanoflakes, nanospheres, urchin-like, and so on) are summarized in Table 3. Here, tungsten-oxide heterostructures are divided into three types according to the different components: (1) semiconductor-WO<sub>x</sub>; (2) WO<sub>x</sub>-C; and (3) metal-WO<sub>x</sub>.

**Table 3.** Application of tungsten oxide-based heterostructured catalysts in water splitting.

Electrocatalyst	Synthesis Method	Electrolyte	Application	Scanning Speed (mV s <sup>-1</sup> )	Overpotential at 10 mA cm <sup>-2</sup> (mV)	Tafel Slope (mV dec <sup>-1</sup> )	Ref.
WO <sub>2</sub> -C nanowires	Calcination	0.5 M H <sub>2</sub> SO <sub>4</sub>	HER	2	58	46	[142]
WO <sub>3</sub> nanoflakes/B-AC	Sonochemical method	1 M KOH	OER	1	320	48	[143]
			HER		360	14	
WO <sub>3</sub> @NPRGO	Redox reaction and carbonization	0.5 M H <sub>2</sub> SO <sub>4</sub>	HER	5	225	87	[144]

Table 3. Cont.

Electrocatalyst	Synthesis Method	Electrolyte	Application	Scanning Speed (mV s <sup>-1</sup> )	Overpotential at 10 mA cm <sup>-2</sup> (mV)	Tafel Slope (mV dec <sup>-1</sup> )	Ref.
Carbon-based shell coated tungsten oxide nanospheres	Hydrothermal method, thermal treatment	1 M NaOH	OER	5	317@50 mA cm <sup>-2</sup>	70	[145]
WO <sub>x</sub> NWs/N-rGO	Hydrothermal method, thermal treatment	0.5 M H <sub>2</sub> SO <sub>4</sub>	HER	2	40	38.2	[146]
WO <sub>x</sub> /C nanowires	Thermal treatment	0.5 M H <sub>2</sub> SO <sub>4</sub>	HER	2	108	46	[147]
Urchin-like CC@WO <sub>3</sub> /Ru SA-450	Hydrothermal–calcining–galvanostatic deposition	0.5 M H <sub>2</sub> SO <sub>4</sub>	HER	2	17	54.7	[136]
		1 M KOH			34	57.5	
		1 M PBS			64	91.9	
NiWO <sub>4</sub> /WO <sub>3</sub> fibers	Electrospinning schematic	0.5 M H <sub>2</sub> SO <sub>4</sub>	HER	1 mA/cm <sup>2</sup>	80	50.27	[132]
		0.1 M KOH			60	41.97	
IrO <sub>2</sub> /WO <sub>3</sub>	Wet-chemical route	0.1 M HClO <sub>4</sub>	OER	10	-	65	[50]
WO <sub>3</sub> -TiO <sub>2</sub> particles	Acid catalyzed peptization method	32% of NaOH	HER	-	120	98	[148]
WS <sub>2</sub> /WO <sub>3</sub> nanosheets	Hydrothermal method	0.5 M H <sub>2</sub> SO <sub>4</sub>	HER	2	395	50	[149]
WO <sub>3</sub> /Ni <sub>3</sub> S <sub>2</sub>	Hydrothermal method, thermal treatment	1 M KOH	HER	5	249@100 mA cm <sup>-2</sup>	45.06	[51]
Ni <sub>17</sub> W <sub>3</sub> /WO <sub>2</sub> nanoparticles	Hydrothermal method, thermal treatment	1 M KOH	HER	5	35	41.6	[150]
W <sub>18</sub> O <sub>49</sub> /NiWO <sub>4</sub>	Hydrothermal method, thermal treatment	1 M KOH	OER	2	250@20 mA cm <sup>-2</sup>	85	[49]
			HER		147@20 mA cm <sup>-2</sup>	101	
WO <sub>3</sub> ·2H <sub>2</sub> O/WS <sub>2</sub>	Anodic treatment	0.5 M H <sub>2</sub> SO <sub>4</sub>	HER	2	152@100 mA cm <sup>-2</sup>	54	[141]
Ni <sub>2</sub> P-WO <sub>3</sub>	Electrodeposition process, phosphating treatment	0.5 M H <sub>2</sub> SO <sub>4</sub>	HER	0.5	107	55.9	[151]
		1 M KOH			105	64.2	
a-WO <sub>x</sub> /WC	Carburization process	0.5 M H <sub>2</sub> SO <sub>4</sub>	HER	5	233@20 mA cm <sup>-2</sup>	69	[52]
		0.1 M PB			292@20 mA cm <sup>-2</sup>	82	
R-Ni <sub>17</sub> W <sub>3</sub> /WO <sub>2</sub>	Hydrothermal method, thermal treatment	1 M KOH	HER	5	48	33	[152]
W <sub>17</sub> O <sub>47</sub> -MoS <sub>2</sub>	Wet chemical, thermal treatment	0.5 M H <sub>2</sub> SO <sub>4</sub>	HER	10	145	41	[57]
WO <sub>2</sub> @C <sub>3</sub> N <sub>4</sub>	Hydrogen thermal process and calcination	0.5 M H <sub>2</sub> SO <sub>4</sub>	HER	5	98	94.4	[36]
MoS <sub>2</sub> @dWO <sub>3</sub>	In situ wet etching	0.5 M H <sub>2</sub> SO <sub>4</sub>	HER	2	191	42	[153]
Fe <sub>2</sub> P-WO <sub>2.92</sub>	Hydrothermal method, thermal treatment	1 M KOH	OER	0.2	215	46.3	[72]
O <sub>v</sub> -WO <sub>x</sub> @NC-Ni	Precursor growth and pyrolysis reaction	1 M KOH	HER	5	67@20 mA cm <sup>-2</sup>	62	[154]
WS <sub>2</sub> /WO <sub>x</sub> /C	Spin-coated and thermal treatment	0.5 M H <sub>2</sub> SO <sub>4</sub>	HER	5	120	36	[155]
Pt@WO <sub>3</sub> /C	Microemulsion method and annealing treatment	1 M PBS	HER	5	149	150	[156]
Ru <sub>2</sub> P/WO <sub>3</sub> /NPC	Hydrothermal method, thermal treatment	1 M KOH	HER	5	15	18	[157]

Table 3. Cont.

Electrocatalyst	Synthesis Method	Electrolyte	Application	Scanning Speed (mV s <sup>-1</sup> )	Overpotential at 10 mA cm <sup>-2</sup> (mV)	Tafel Slope (mV dec <sup>-1</sup> )	Ref.
(Co <sub>5.47</sub> N-CO <sub>2</sub> )@C	Hydrothermal method, thermal treatment	1 M KOH	HER	5	36	68	[158]
			OER		270	60	
			OWS		1.54	-	
WO <sub>3</sub> @F-GS	Plasma-induced assembly method	1 M KOH	OER	5	298	77.6	[133]
CoSe <sub>2</sub> /WSe <sub>2</sub> /WO <sub>3</sub> NWs	Hydrothermal method, thermal treatment	1 M KOH	HER	5	115	121	[159]
Ru/N-doped Carbon@WO <sub>3</sub> -W <sub>2</sub> C	Co-precipitation method and polyol reduction method	1 M KOH	HER	-	31	40.5	[160]
NiWO <sub>4</sub> -WO <sub>3</sub> -WO <sub>2.9</sub>	Electrospinning method, thermal treatment	0.5 M H <sub>2</sub> SO <sub>4</sub>	HER	2	40	69	[53]
		0.1 M KOH			50	45	
rGO/WS <sub>2</sub> /WO <sub>3</sub>	One-step aerosolization	0.5 M H <sub>2</sub> SO <sub>4</sub>	HER	-	113	37	[161]
WNi <sub>4</sub> @W-WO <sub>2</sub>	Hydrothermal method, thermal treatment	1 M KOH	HER	-	83	83	[162]
Pt <sub>2</sub> W/WO <sub>3</sub> /RGO	Co-deposition	0.5 M H <sub>2</sub> SO <sub>4</sub>	HER	5	394@500 mA cm <sup>-2</sup>	36.8	[163]
2D-Ni(Co,Fe)P/1D-WO <sub>x</sub>	Thermal evaporation–electrodeposition–thermal treatment	1 M KOH	HER	2	49	108	[164]
			OER		270	351	
			OWS		1.51 V	-	
N-doped graphene/WSe <sub>2</sub> -WO <sub>3</sub>	Liquid-phase physical co-exfoliation and heat treatment	0.5 M H <sub>2</sub> SO <sub>4</sub>	HER	5	257	101.9	[165]
WO <sub>2</sub> -Na <sub>x</sub> WO <sub>3</sub> @FeOOH/NF	Hydrothermal method, thermal treatment, FeOOH coating	1 M KOH	OER	1	220@20 mA cm <sup>-2</sup>	42.2	[166]
TA-Fe@Ni-WO <sub>x</sub>	Hydrothermal method, thermal treatment-FeOOH coating	1 M KOH	HER	2	240@20 mA cm <sup>-2</sup>	63.37	[167]
Fe-WO <sub>x</sub> P/rGO	Hydrothermal, CVD method	0.5 M H <sub>2</sub> SO <sub>4</sub>	HER	2	54.6	41.99	[168]
WO <sub>(3-x)</sub> -WC <sub>y</sub> /CDs	Hydrothermal method	0.5 M H <sub>2</sub> SO <sub>4</sub>	HER	5	65	50	[140]
SiO <sub>2</sub> /WO <sub>3</sub> /NiWO <sub>4</sub>	Electrospinning method, carbonization process	0.5 M H <sub>2</sub> SO <sub>4</sub>	HER	2	320	48	[169]
Pt-WO <sub>3</sub> /rGO aerogel	Solvothermal method, electrodeposition	0.5 M H <sub>2</sub> SO <sub>4</sub>	HER	5	42	30	[71]
WS <sub>2</sub> -WC-WO <sub>3</sub> NHs	Hydrothermal method	0.5 M H <sub>2</sub> SO <sub>4</sub>	HER	5	352	59	[170]
NC/Vo-WON	Hydrothermal and hydrogenation/nitridation-induced strategy	1 M KOH	HER	2	16	33	[171]
WO <sub>x</sub> -PtNi@Pt DNWs	Wet-chemical method	0.1 M KOH	HER	10	24	-	[55]
		0.1 M HClO <sub>4</sub>			5		
		0.5 M PBS			22		

### 5.1. Semiconductor–WO<sub>x</sub>

The interaction between tungsten oxide and another semiconductor is conducive to adjusting its electronic structure. When tungsten oxide comes into contact with a semiconductor with different Fermi levels, the electrons will spontaneously diffuse from the

semiconductor with a high Fermi level to another component until the chemical potential of the two parts is equal, thus forming a semiconductor– $\text{WO}_x$  heterojunction structure [172]. Consequently, net charges accumulate at the contacting interface, which lowers the initially higher Fermi level and raises the initial lower Fermi level. Meanwhile, the electronic band of the contacting semiconductor bends over subject to the movement of Fermi levels, generating different types of band alignments. Due to the synergistic effect and electronic effect between the components, the catalytic performance of the composites is improved. Wang and his colleagues prepared the  $\text{Ni}_2\text{P}$ – $\text{WO}_3$  nanoneedle structure on carbon cloth using a combination of in situ electrodeposition and phosphating treatment methods [151]. The XPS results demonstrate the electrons transfer from Ni to P in  $\text{Ni}_2\text{P}$ – $\text{WO}_3$ . Benefiting from the heterojunction structure,  $\text{Ni}_2\text{P}$ – $\text{WO}_3$  exhibits excellent HER catalytic performance in both acidic (over-potential of 107 mV at a current density of  $10 \text{ mA cm}^{-2}$ ) and alkaline (over-potential of 105 mV at a current density of  $10 \text{ mA cm}^{-2}$ ) environments. Peng et al. designed a  $\text{Fe}_2\text{P}$ – $\text{WO}_{2.92}$  heterostructure on nickel foam by a facile consecutive three-step synthesis method [72]. The oxygen vacancies and the synergistic effect between  $\text{WO}_{2.92}$  and  $\text{Fe}_2\text{P}$  facilitated a drastic reduction in over-potential for the catalytic OER performance of  $\text{Fe}_2\text{P}$ – $\text{WO}_{2.92}$ /NF (over-potential of 215 mV at  $10 \text{ mA cm}^{-2}$  in 1.0 M KOH solution).

Moreover, the interfacial richness of the two phases in the semiconductor– $\text{WO}_x$  heterostructure directly affects the number of active sites. Yang's group prepared  $\text{Ni}_{17}\text{W}_3$ / $\text{WO}_2$  heterojunction on nickel foam ( $\text{WO}_2$ /Ni<sub>17</sub>W<sub>3</sub>/NF) by the hydrothermal and annealing method (Figure 9a) [150].  $\text{WO}_2$ /Ni<sub>17</sub>W<sub>3</sub> heterojunctions increase the exposure of active edge sites and facilitate the water dissociation and H intermediates association during HER kinetics. Therefore,  $\text{WO}_2$ /Ni<sub>17</sub>W<sub>3</sub>/NF demonstrated high catalytic efficiency for HER with a low over-potential of 35 mV at  $10 \text{ mA cm}^{-2}$ . Following this work, Liu's group prepared R-Ni<sub>17</sub>W<sub>3</sub>/ $\text{WO}_2$  catalysts on Ni foam and explored the effect of Ni<sub>17</sub>W<sub>3</sub> particle size decorated on the NiWO<sub>4</sub>/ $\text{WO}_2$  substrate for hydrogen evolution reaction (Figure 9b) [152]. The R-Ni<sub>17</sub>W<sub>3</sub>/ $\text{WO}_2$  with larger Ni<sub>17</sub>W<sub>3</sub> particles exhibited superior HER catalytic activity (over-potential of 48 mV at  $10 \text{ mA cm}^{-2}$ ), resulting from more interfaces and more active sites (Figure 9c). For R-Ni<sub>17</sub>W<sub>3</sub>/ $\text{WO}_2$ /NiWO<sub>4</sub>, H<sub>2</sub>O adsorption/deionization occurred at the Ni<sub>17</sub>W<sub>3</sub>/NiWO<sub>4</sub> interface, and H<sub>ads</sub> and OH<sub>ads</sub> were adsorbed on Ni<sub>17</sub>W<sub>3</sub> and NiWO<sub>4</sub>, respectively. The H<sub>ads</sub> on Ni<sub>17</sub>W<sub>3</sub> overflow to  $\text{WO}_2$  preferentially in Ni<sub>17</sub>W<sub>3</sub>/ $\text{WO}_2$  interface, which is conducive to the desorption of H<sub>2</sub> (Figure 9d). Our group also prepared a TA-Fe@Ni– $\text{WO}_x$  hierarchical structure by the interfacial coordination assembly process. After the introduction of the TA-Fe layer, the electrons transfer from W and Ni to TA-Fe, and as a result, the TA-Fe@Ni– $\text{WO}_x$  has an upward-moving Fermi energy, a smaller ionization potential, and a more electron-rich environment, which is more conducive to OER [167].

## 5.2. $\text{WO}_x$ –C

Creating a heterostructure with another conductive material is a typical way to increase the electrocatalyst's overall electronic conductivity. Carbon materials, including graphene oxide (GO), carbon nanotube (CNT), carbon paper, and carbon cloth, are often used due to their superior electronic conductivity, high specific surface area, and excellent chemical durability [56,173–176].  $\text{WO}_x$ /carbon composites have been widely used in electrocatalytic water splitting [71,142,143,145,146,177]. In this case, carbon-encapsulated  $\text{WO}_x$  with rich oxygen vacancies was synthesized by pyrolyzing carbon/tungsten mixture (Figure 10a,b) [95,144,178,179], which has a favorable impact on enhancing charge transfer and compensating for the weak hydrogen adsorption of the tungsten oxide. The effects of W content [95], annealing time [179], and annealing temperature [178] on HER performance of  $\text{WO}_x$ /C have been deeply explored. For example, Yin et al. studied the effects of different annealing times and temperatures on hydrogen evolution properties of  $\text{WO}_x$ /C in 0.5 M H<sub>2</sub>SO<sub>4</sub> (Figure 10c) [179]. Pan's group introduced 15 nm thick carbon-based shells on the surface of tungsten oxide nanospheres (CTO) and investigated its catalytic performance in alkaline OER [145]. It was found that the overpotential of nanoparticles at  $50 \text{ mA cm}^{-2}$  decreased from 360 to 317 mV after the introduction of a carbon-based shell (Figure 10d).

The improved catalytic performance is attributed to the carbon-based shell that speeds up the electron transfer between the catalyst and the reactant, provides the catalytic active site, and promotes the adsorption of the catalyst to the reactant and the dissociation of the O–H bond.

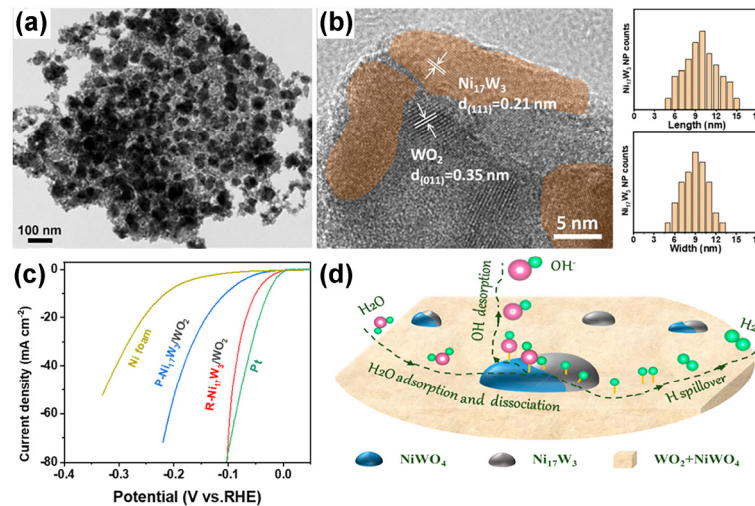


**Figure 9.** (a) TEM image of the  $\text{Ni}_{17}\text{W}_3/\text{WO}_2$ . Reprinted with permission from Reprinted with permission from [150], with permission from the American Chemical Society, 2019. (b) HRTEM image and size distribution plots for R- $\text{Ni}_{17}\text{W}_3/\text{WO}_2$  nanoparticles. (c) Polarization curves for Pt foil, Ni foam, P- $\text{Ni}_{17}\text{W}_3/\text{WO}_2$ , and R- $\text{Ni}_{17}\text{W}_3/\text{WO}_2$ . (d) Schematic diagram of R- $\text{Ni}_{17}\text{W}_3/\text{WO}_2$  nanoparticles accelerating the rate of hydrogen evolution reaction. Reprinted with permission from [152], with permission from the American Chemical Society, 2021.

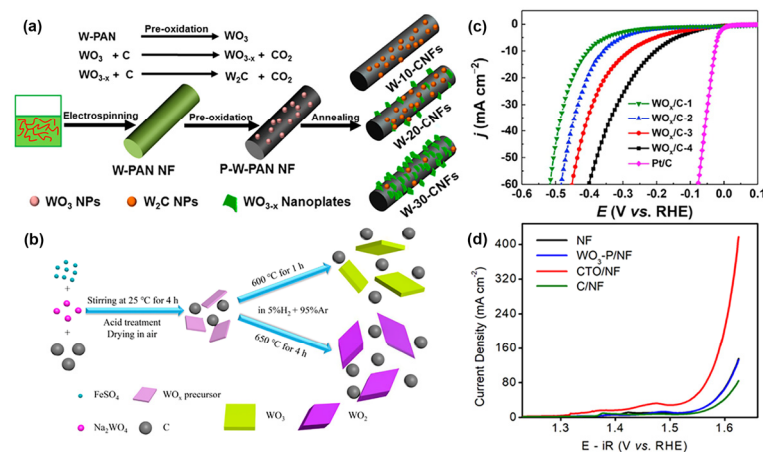


**Figure 10.** (a) Schematic diagram of  $\text{WO}_{3-x}$  synthesis. Reprinted with permission from [95], with permission from the American Chemical Society, 2016. (b) Schematic diagram of  $\text{WO}_x/\text{C}$  synthesis steps. (c) Polarization curves with  $iR$  compensation of the  $\text{WO}_x/\text{C}$  in 0.5 M  $\text{H}_2\text{SO}_4$  aqueous solution. Reprinted with permission from [179], with permission from Elsevier, 2021. (d) LSV polarization curves measured at a scan rate of  $5 \text{ mV s}^{-1}$  in 1 M NaOH. Reprinted with permission from [145], with permission from the American Chemical Society, 2020.

### 5.3. Metal- $\text{WO}_x$

Conductive metal is also widely used to increase the electrocatalyst's overall electronic conductivity and adjust the electronic structure of  $\text{WO}_x$ . In order to reduce the cost of the catalyst, the metal part in metal- $\text{WO}_x$  heterostructure often exists in the form of single atoms, clusters, or nanoparticles [71,120,156]. Li et al. prepared Pt@ $\text{WO}_3/\text{C}$  with three-dimensional nano architectures for HER via the water–oil two-phase microemulsion

method and the annealing treatment [156]. Pt nanoparticles with a diameter of about 4 nm were monodispersed on the surface of WO<sub>3</sub>/C structures (Figure 11a,b). The overpotential at 10 mA cm<sup>-2</sup> of Pt@WO<sub>3</sub>/C as HER electrocatalyst was 149 mV (Figure 11c), which was smaller than that of WO<sub>3</sub>/C (244 mV). The mechanism of HER consists of three main steps, including H<sub>2</sub>O adsorption, H<sub>2</sub>O dissociation, and H<sup>\*</sup> desorption (Figure 11d). The corresponding free energy calculation results show that the introduction of Pt has no obvious effect on water absorption, but it can promote the water dissociation and H<sup>\*</sup> desorption of WO<sub>3</sub>, thus accelerating the HER process (Figure 11e). The XPS results (Figure 11f) also confirm that the peaks of W 4f were positively shifted after the introduction of Pt due to the difference in electronegativity between W and Pt atoms, resulting in the transfer of electrons from W to Pt. In another work, Pt-WO<sub>3-x</sub> nanodots were anchored on rGO for water splitting [37]. The optimized composite Pt-WO<sub>3-x</sub>@rGO exhibited the highest HER, OER, and overall water-splitting activities in alkaline environments (overpotentials of about 34 mV, 174 mV, and 1.55 V at 10 mA cm<sup>-2</sup>, respectively). At the same time, its overall water-splitting performance showed excellent durability at 1.55 V, where 93.3% initial potential could be maintained after 14 h of cycling.

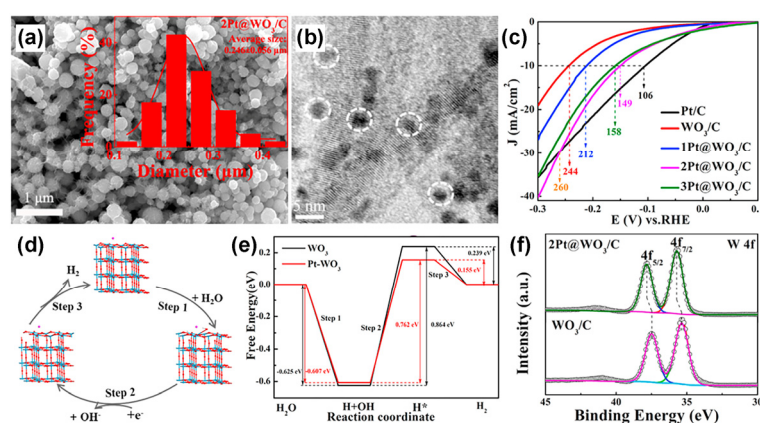


**Figure 11.** (a) FESEM and (b) HRTEM images of 2Pt@WO<sub>3</sub>/C. Insert of (a) is the size distribution. The white circle in (b) are Pt particles. (c) The polarization curves of WO<sub>3</sub>/C, 1Pt@WO<sub>3</sub>/C, 2Pt@WO<sub>3</sub>/C, and 3Pt@WO<sub>3</sub>/C. (d) the HER process and corresponding chemisorption models of Pt-WO<sub>3</sub> in neutral media, and (e) the corresponding free energy level diagram. (f) XPS of WO<sub>3</sub>/C and 2Pt@WO<sub>3</sub>/C. Reprinted with permission from [156], with permission from Elsevier, 2022.

## 6. Summary and Outlook

In this review, we focus on the recent research progress of tungsten oxide-based nanomaterials for water splitting, especially revealing the mechanism of structural design and component regulation to improve the electrocatalytic performances, which is expected to guide the preparation of high-performance tungsten oxide-based electrocatalysts. The practical strategies for improving the performance of tungsten-oxide catalysts are discussed in this review. The band gap and contact area of a tungsten oxide-based electrode can be adjusted by controlling the morphology and crystal phase, thus improving its catalytic performance. The electronic structure of WO<sub>x</sub> can also be optimized through defect engineering to provide more active sites and an excellent electronic environment for catalytic reactions. Additionally, the synergistic effect can boost the electron transfer of tungsten oxide and provide more active boundaries, which is another commonly used effective strategy for enhancing catalytic performance. Due to the adjustment of structure and composition, noble metal single atom/tungsten oxide/carbon, the best tungsten-based catalyst at present, greatly reduces the cost on the premise of excellent catalytic performance. Despite the advancement of these methods, the practical application of tungsten-based materials in water splitting is still in the early stage, and there are still many problems and challenges.

First, defect engineering has been widely used in regulating the electronic structure of tungsten oxide and promoting its catalytic performance. However, the precise control of the defect location and concentration is difficult, and the characterization technology of defect types and concentration is insufficient. Therefore, the improvement of catalytic performance by defect engineering lacks an intrinsic understanding. The development and utilization of more advanced in situ preparation and characterization technologies may somewhat solve this problem. For example, in situ atmospheric spherical correction transmission electron microscopy can be used to directly observe the defect formation process in nanomaterials and the resulting crystal phase changes.

Besides, the current research on the structure–property relationship mainly adopts the post-analysis method, which compares the electrocatalyst’s structure before and after the catalytic reaction and infers the structure evolution during the reaction based on the static characterization results. However, the structure of tungsten oxide dynamically evolves in the catalytic reaction process. The morphology, chemical composition, and electronic structure of tungsten oxide are constantly changing and recycling. As a result, the structure differences before and after long-lasting catalytic reactions may not reflect the real active sites. To further understand the structure–property mechanism of tungsten oxide-based electrocatalysts, it is necessary to develop and utilize in situ characterization methods, such as in situ electron microscope and the in situ XRD technique, to record the dynamic structural changes of the catalysts in real-time during the reaction.

We believe that the growth mechanism of material preparation and structure–property relationship can be better understood by in situ observation of the structure and defect location and concentration, as well as in situ characterization of catalytic processes. Combined with advanced theoretical simulation techniques, it is possible to obtain tungsten oxide-based electrocatalysts with high intrinsic activity. All these developments will significantly contribute to the rapid development of renewable energy storage and conversion.

**Author Contributions:** Y.W. did the writing and literature research for the paper. S.D. contributed to conception, and conceptualization. R.W. guided and supervised the work. All authors have read and agreed to the published version of the manuscript.

**Funding:** This research was funded by the Beijing Natural Science Foundation (No. 2212034), the National Natural Science Foundation of China (Nos. 12034002 and 51971025), and the 111 Project (No. B170003).

**Data Availability Statement:** In this review manuscript, no new data were created.

**Conflicts of Interest:** The authors declare no conflict of interest.

## References

1. Xue, S.; Zhang, W.; Zhang, Q.; Du, J.; Cheng, H.-M.; Ren, W. Heterostructured Ni-Mo-N nanoparticles decorated on reduced graphene oxide as efficient and robust electrocatalyst for hydrogen evolution reaction. *Carbon* **2020**, *165*, 122–128. [[CrossRef](#)]
2. Zhang, D.; Zhao, H.; Huang, B.; Li, B.; Li, H.; Han, Y.; Wang, Z.; Wu, X.; Pan, Y.; Sun, Y.; et al. Advanced ultrathin RuPdM (M = Ni, Co, Fe) nanosheets electrocatalyst boosts hydrogen evolution. *ACS Cent. Sci.* **2019**, *5*, 1991–1997. [[CrossRef](#)] [[PubMed](#)]
3. Tan, Y.; Che, Q.; Li, Q. Constructing double-layer CoP/CeO<sub>2</sub>-FeO<sub>x</sub>H hybrid catalysts for alkaline and neutral water splitting. *ACS Sustain. Chem. Eng.* **2021**, *9*, 11981–11990. [[CrossRef](#)]
4. Shao, X.; Liang, M.; Kumar, A.; Liu, X.; Jin, H.; Ajmal, S.; Bui, V.Q.; Bui, H.T.D.; Lee, J.; Tran, N.Q.; et al. Amorphization of metal nanoparticles by 2D twisted polymer for super hydrogen evolution reaction. *Adv. Energy Mater.* **2022**, *12*, 2102257. [[CrossRef](#)]
5. Yang, M.; Zhang, C.H.; Li, N.W.; Luan, D.; Yu, L.; Lou, X.W. Design and synthesis of hollow nanostructures for electrochemical water splitting. *Adv. Sci.* **2022**, *9*, 2105135. [[CrossRef](#)]
6. Zhang, X.-Y.; Yu, W.-L.; Zhao, J.; Dong, B.; Liu, C.-G.; Chai, Y.-M. Recent development on self-supported transition metal-based catalysts for water electrolysis at large current density. *Appl. Mater. Today* **2021**, *22*, 100913. [[CrossRef](#)]
7. Coles, D.; Wray, B.; Stevens, R.; Crawford, S.; Pennock, S.; Miles, J. Impacts of tidal stream power on energy system security: An Isle of Wight case study. *Appl. Energy* **2023**, *334*, 120686. [[CrossRef](#)]
8. Gao, C.Y.; Yu, X.Y.; Nan, H.P.; Zhang, Z.Y.; Wu, L.C.; Men, C.; Cai, Q.S. Advancement and capacity allocation analysis of variable speed hydropower units for suppressing wind power fluctuations. *Front. Energy Res.* **2023**, *10*, 1030797. [[CrossRef](#)]

9. Kakoulaki, G.; Sanchez, R.G.; Amillo, A.G.; Szabo, S.; De Felice, M.; Farinosi, F.; De Felice, L.; Bisselink, B.; Seliger, R.; Kougiyas, I.; et al. Benefits of pairing floating solar photovoltaics with hydropower reservoirs in Europe. *Renew. Sustain. Energy Rev.* **2023**, *171*, 112989. [[CrossRef](#)]
10. Ogunjo, S.; Olusola, A.; Olusegun, C. Potential of using floating solar photovoltaic and wind farms for sustainable energy generation in an existing hydropower station in Nigeria. *Clean Technol. Environ. Policy* **2023**. [[CrossRef](#)]
11. Xiao, L.; Wang, J.; Wang, B.L.; Jiang, H. China's hydropower resources and development. *Sustainability* **2023**, *15*, 3940. [[CrossRef](#)]
12. Morales-Guio, C.G.; Tilley, S.D.; Vrubel, H.; Grätzel, M.; Hu, X. Hydrogen evolution from a copper(I) oxide photocathode coated with an amorphous molybdenum sulphide catalyst. *Nat. Commun.* **2014**, *5*, 3059. [[CrossRef](#)] [[PubMed](#)]
13. Jiang, E.; Li, J.; Li, X.; Ali, A.; Wang, G.; Ma, S.; Zhu, J.; Shen, P.K. MoP-Mo<sub>2</sub>C quantum dot heterostructures uniformly hosted on a heteroatom-doped 3D porous carbon sheet network as an efficient bifunctional electrocatalyst for overall water splitting. *Chem. Eng. J.* **2022**, *431*, 133719. [[CrossRef](#)]
14. Balat, M. Potential importance of hydrogen as a future solution to environmental and transportation problems. *Int. J. Hydrogen Energy* **2008**, *33*, 4013–4029. [[CrossRef](#)]
15. Escalera-López, D.; Cziotka, S.; Geppert, J.; Boubnov, A.; Röse, P.; Saraçi, E.; Krewer, U.; Grunwaldt, J.-D.; Cherevko, S. Phase- and surface composition-dependent electrochemical stability of Ir-Ru nanoparticles during oxygen evolution reaction. *ACS Catal.* **2021**, *11*, 9300–9316. [[CrossRef](#)]
16. da Silva Veras, T.; Mozer, T.S.; da Costa Rubim Messeder dos Santos, D.; da Silva César, A. Hydrogen: Trends, production and characterization of the main process worldwide. *Int. J. Hydrogen Energy* **2017**, *42*, 2018–2033. [[CrossRef](#)]
17. Dawood, F.; Anda, M.; Shafiullah, G.M. Hydrogen production for energy: An overview. *Int. J. Hydrogen Energy* **2020**, *45*, 3847–3869. [[CrossRef](#)]
18. Yuan, H.; Wang, S.; Ma, Z.; Kundu, M.; Tang, B.; Li, J.; Wang, X. Oxygen vacancies engineered self-supported B doped Co<sub>3</sub>O<sub>4</sub> nanowires as an efficient multifunctional catalyst for electrochemical water splitting and hydrolysis of sodium borohydride. *Chem. Eng. J.* **2021**, *404*, 126474. [[CrossRef](#)]
19. Ma, Y.; Chen, M.; Geng, H.; Dong, H.; Wu, P.; Li, X.; Guan, G.; Wang, T. Synergistically tuning electronic structure of porous β-Mo<sub>2</sub>C spheres by Co doping and Mo-vacancies defect engineering for optimizing hydrogen evolution reaction activity. *Adv. Funct. Mater.* **2020**, *30*, 2000561. [[CrossRef](#)]
20. Zhao, D.; Dai, M.; Liu, H.; Duan, Z.; Tan, X.; Wu, X. Bifunctional ZnCo<sub>2</sub>S<sub>4</sub>@CoZn<sub>13</sub> hybrid electrocatalysts for high efficient overall water splitting. *J. Energy Chem.* **2022**, *69*, 292–300. [[CrossRef](#)]
21. Shrestha, N.K.; Patil, S.A.; Han, J.; Cho, S.; Inamdar, A.I.; Kim, H.; Im, H. Chemical etching induced microporous nickel backbones decorated with metallic Fe@hydroxide nanocatalysts: An efficient and sustainable OER anode toward industrial alkaline water-splitting. *J. Mater. Chem. A* **2022**, *10*, 8989–9000. [[CrossRef](#)]
22. Kibsgaard, J.; Chorkendorff, I. Considerations for the scaling-up of water splitting catalysts. *Nat. Energy* **2019**, *4*, 430–433. [[CrossRef](#)]
23. You, B.; Sun, Y. Innovative strategies for electrocatalytic water splitting. *ACC. Chem. Res.* **2018**, *51*, 1571–1580. [[CrossRef](#)] [[PubMed](#)]
24. Wu, X.; Chen, J.; Wen, Z. Promotion for full water splitting toward vanadium-incorporated MoO<sub>2</sub>-MoNi<sub>4</sub> hybrid nanoarrays. *ACS Sustain. Chem. Eng.* **2021**, *9*, 13225–13232. [[CrossRef](#)]
25. Ali, A.; Long, F.; Shen, P.K. Innovative strategies for overall water splitting using nanostructured transition metal electrocatalysts. *Electrochem. Energy Rev.* **2022**, *6*, 1. [[CrossRef](#)]
26. Al-Naggar, A.H.; Shinde, N.M.; Kim, J.-S.; Mane, R.S. Water splitting performance of metal and non-metal-doped transition metal oxide electrocatalysts. *Coord. Chem. Rev.* **2023**, *474*, 214864. [[CrossRef](#)]
27. Zhou, Y.; Hu, X.C.; Liu, X.H.; Wen, H.R. Core-shell hierarchical WO<sub>2</sub>/WO<sub>3</sub> microsphere as an electrocatalyst support for methanol electrooxidation. *Chem. Comm.* **2015**, *51*, 15297–15299. [[CrossRef](#)] [[PubMed](#)]
28. Huang, Z.F.; Song, J.; Pan, L.; Zhang, X.; Wang, L.; Zou, J.J. Tungsten oxides for photocatalysis, electrochemistry, and phototherapy. *Adv. Mater.* **2015**, *27*, 5309–5327. [[CrossRef](#)]
29. Diao, J.; Yuan, W.; Qiu, Y.; Cheng, L.; Guo, X. A hierarchical oxygen vacancy-rich WO<sub>3</sub> with “nanowire-array-on-nanosheet-array” structure for highly efficient oxygen evolution reaction. *J. Mater. Chem. A* **2019**, *7*, 6730–6739. [[CrossRef](#)]
30. Zheng, J.Y.; Song, G.; Hong, J.; Van, T.K.; Pawar, A.U.; Kim, D.Y.; Kim, C.W.; Haider, Z.; Kang, Y.S. Facile fabrication of WO<sub>3</sub> nanoplates thin films with dominant crystal facet of (002) for water splitting. *Cryst. Growth Des.* **2014**, *14*, 6057–6066. [[CrossRef](#)]
31. Jiang, M.; Zhang, G.; Li, C.; Liu, J.; Guo, K.; Ning, H.; Shi, M.; Guo, D.; Yao, R.; Peng, J. Effects of rapid thermal annealing on wide band gap tungsten oxide films. *Super. Microstruct.* **2020**, *142*, 106541. [[CrossRef](#)]
32. Johansson, M.B.; Kristiansen, P.T.; Duda, L.; Niklasson, G.A.; Osterlund, L. Band gap states in nanocrystalline WO<sub>3</sub> thin films studied by soft X-ray spectroscopy and optical spectrophotometry. *J. Phys. Condens. Matter* **2016**, *28*, 475802. [[CrossRef](#)] [[PubMed](#)]
33. Chen, X.Y.; Yang, J.; Cao, Y.F.; Kong, L.; Huang, J.F. Design principles for tungsten oxide electrocatalysts for water splitting. *ChemElectroChem* **2021**, *8*, 4427–4440. [[CrossRef](#)]
34. Zhu, L.; Zhang, Z.; Ke, X.; Wang, J.; Perepezko, J.; Sui, M. WO<sub>2</sub> triggered nucleation and growth of ultra-long W<sub>18</sub>O<sub>49</sub> structures, from nanobundles to single-crystalline microrod. *Acta Mater.* **2018**, *148*, 55–62. [[CrossRef](#)]

35. Cheng, H.; Klapproth, M.; Sagaltchik, A.; Li, S.; Thomas, A. Ordered mesoporous WO<sub>2.83</sub>: Selective reduction synthesis, exceptional localized surface plasmon resonance and enhanced hydrogen evolution reaction activity. *J. Mater. Chem. A* **2018**, *6*, 2249–2256. [[CrossRef](#)]
36. Lu, S.-S.; Zhang, L.-M.; Fan, K.; Xie, J.-Y.; Shang, X.; Zhang, J.-Q.; Chi, J.-Q.; Yang, X.-L.; Wang, L.; Chai, Y.-M.; et al. In situ formation of ultrathin C<sub>3</sub>N<sub>4</sub> layers on metallic WO<sub>2</sub> nanorods for efficient hydrogen evolution. *Appl. Surf. Sci.* **2019**, *487*, 945–950. [[CrossRef](#)]
37. Yin, D.; Cao, Y.-D.; Chai, D.-F.; Fan, L.-L.; Gao, G.-G.; Wang, M.-L.; Liu, H.; Kang, Z. A WO<sub>x</sub> mediated interface boosts the activity and stability of Pt-catalyst for alkaline water splitting. *Chem. Eng. J.* **2022**, *431*, 133287–133297. [[CrossRef](#)]
38. Qian, K.; Du, L.; Zhu, X.; Liang, S.; Chen, S.; Kobayashi, H.; Yan, X.; Xu, M.; Dai, Y.; Li, R. Directional oxygen activation by oxygen-vacancy-rich WO<sub>2</sub> nanorods for superb hydrogen evolution via formaldehyde reforming. *J. Mater. Chem. A* **2019**, *7*, 14592–14601. [[CrossRef](#)]
39. Zhu, K.; Shi, F.; Zhu, X.; Yang, W. The roles of oxygen vacancies in electrocatalytic oxygen evolution reaction. *Nano Energy* **2020**, *73*, 104761. [[CrossRef](#)]
40. Han, H.; Nayak, A.K.; Choi, H.; Ali, G.; Kwon, J.; Choi, S.; Paik, U.; Song, T. Partial dehydration in hydrated tungsten oxide nanoplates leads to excellent and robust bifunctional oxygen reduction and hydrogen evolution reactions in acidic media. *ACS Sustain. Chem. Eng.* **2020**, *8*, 9507–9518. [[CrossRef](#)]
41. Yang, J.; Chen, X.Y.; Liu, X.Y.; Cao, Y.F.; Huang, J.F.; Li, Y.S.; Liu, F. From hexagonal to monoclinic: Engineering crystalline phase to boost the intrinsic catalytic activity of tungsten oxides for the hydrogen evolution reaction. *ACS Sustain. Chem. Eng.* **2021**, *9*, 5642–5650. [[CrossRef](#)]
42. Zhang, X.; Jin, G.; Wang, D.; Chen, Z.; Zhao, M.; Xi, G. Crystallographic phase and morphology dependent hydrothermal synthesis of tungsten oxide for robust hydrogen evolution reaction. *J. Alloys Compd.* **2021**, *875*, 160054. [[CrossRef](#)]
43. Li, Q.; Wang, L.; Ai, X.; Chen, H.; Zou, J.; Li, G.D.; Zou, X. Multiple crystal phases of intermetallic tungsten borides and phase-dependent electrocatalytic property for hydrogen evolution. *Chem. Commun.* **2020**, *56*, 13983–13986. [[CrossRef](#)] [[PubMed](#)]
44. Rajalakshmi, R.; Rebekah, A.; Viswanathan, C.; Ponpandian, N. Evolution of intrinsic 1-3D WO<sub>3</sub> nanostructures: Tailoring their phase structure and morphology for robust hydrogen evolution reaction. *Chem. Eng. J.* **2022**, *428*, 132013–132030.
45. Wang, J.; Liao, T.; Wei, Z.; Sun, J.; Guo, J.; Sun, Z. Heteroatom-doping of non-noble metal-based catalysts for electrocatalytic hydrogen evolution: An electronic structure tuning strategy. *Small Methods* **2021**, *5*, 2000988. [[CrossRef](#)]
46. Xue, Z.; Liu, Y.; Liu, Q.; Zhang, Y.; Yu, M.; Liang, Q.; Hu, J.; Li, G. Constructing nickel sulfide heterojunctions by W-doping-induced structural transition for enhanced oxygen evolution. *J. Mater. Chem. A* **2022**, *10*, 3341–3345. [[CrossRef](#)]
47. Wang, R.; Yang, Y.; Sun, Z.; Lu, X. Ga doped Ni<sub>3</sub>S<sub>2</sub> ultrathin nanosheet arrays supported on Ti<sub>3</sub>C<sub>2</sub>-MXene/Ni foam: An efficient and stable 3D electrocatalyst for oxygen evolution reaction. *Int. J. Hydrogen Energy* **2022**, *47*, 2958–2966. [[CrossRef](#)]
48. Huang, H.; Xu, L.; Yoon Woo, D.; Kim, S.; Min Kim, S.; Kyeong Kim, Y.; Byeon, J.; Lee, J. Refining the surface properties of WO<sub>2.7</sub> by vacancy engineering and transition metals doping for enhanced alkaline hydrogen evolution reaction. *Chem. Eng. J.* **2023**, *451*, 138939. [[CrossRef](#)]
49. Hai, G.; Huang, J.; Cao, L.; Kajiyoshi, K.; Wang, L.; Feng, L. Hierarchical W<sub>18</sub>O<sub>49</sub>/NiWO<sub>4</sub>/NF heterojunction with tuned composition and charge transfer for efficient water splitting. *Appl. Surf. Sci.* **2021**, *562*, 150145. [[CrossRef](#)]
50. Tariq, M.; Zaman, W.Q.; Wu, Y.Y.; Nabi, A.; Abbas, Z.; Iqbal, W.; Sun, W.; Hao, Z.; Zhou, Z.H.; Cao, L.M.; et al. Facile synthesis of IrO<sub>2</sub> nanoparticles decorated@WO<sub>3</sub> as mixed oxide composite for outperformed oxygen evolution reaction. *Int. J. Hydrogen Energy* **2019**, *44*, 31082–31093. [[CrossRef](#)]
51. Sun, T.M.; Zhong, W.T.; Zhang, M.K.; Tang, Y.F.; Wang, J.; Xu, C.; Hu, L.P.; Wang, M.M. A low-cost 2D WO<sub>3</sub>/Ni<sub>3</sub>S<sub>2</sub> heterojunction for highly stable hydrogen evolution. *Mater. Chem. Front.* **2021**, *5*, 8248–8254. [[CrossRef](#)]
52. Cui, Y.L.S.; Tan, X.; Xiao, K.F.; Zhao, S.L.; Bedford, N.M.; Liu, Y.F.; Wang, Z.C.; Wu, K.H.; Pan, J.; Saputera, W.H.; et al. Tungsten oxide/carbide surface heterojunction catalyst with high hydrogen evolution activity. *ACS Energy Lett.* **2020**, *5*, 3560–3568. [[CrossRef](#)]
53. Anis, S.F.; Mostafa, A.O.; Hilal, N.; Hashaikeh, R. Nanocrystalline NiWO<sub>4</sub>-WO<sub>3</sub>-WO<sub>2.9</sub> composite strings: Fabrication, characterization and their electrocatalytic performance for hydrogen evolution reaction. *Metall. Mater. Trans. A Phys. Metall. Mater. Sci.* **2020**, *51*, 1264–1274. [[CrossRef](#)]
54. Fominski, V.; Gnedovets, A.; Fominski, D.; Romanov, R.; Kartsev, P.; Rubinkovskaya, O.; Novikov, S. Pulsed laser deposition of nanostructured MoS<sub>3</sub>/NP-Mo//WO<sub>3-y</sub> hybrid catalyst for enhanced (photo) electrochemical hydrogen evolution. *Nanomaterials* **2019**, *9*, 1395. [[CrossRef](#)] [[PubMed](#)]
55. Zhang, W.; Huang, B.; Wang, K.; Yang, W.; Lv, F.; Li, N.; Chao, Y.; Zhou, P.; Yang, Y.; Li, Y.; et al. WO<sub>x</sub>-surface decorated PtNi@Pt dendritic nanowires as efficient pH-universal hydrogen evolution electrocatalysts. *Adv. Energy Mater.* **2021**, *11*, 2003192. [[CrossRef](#)]
56. Liu, J.; Zhang, T.; Liu, T.; Liu, K.; Tan, X.; Yu, X.; Zhao, Q. Oxygen vacancy-rich WO<sub>3-x</sub>/rGO composite supported Pd catalyst for efficient selective hydrogenation of nitroaromatics. *J. Alloys Compd.* **2023**, *932*, 167577. [[CrossRef](#)]
57. Jiang, R.; He, C.; Guo, C.; Chen, W.; Luo, J.; Chen, Y.; Wang, L. Edge-contact geometry and anion-deficit construction for activating ultrathin MoS<sub>2</sub> on W<sub>17</sub>O<sub>47</sub> in the hydrogen evolution reaction. *Inorg. Chem.* **2019**, *58*, 11241–11247. [[CrossRef](#)]
58. Kumar, S.; Soni, R.; Kurungot, S. PdP/WO<sub>3</sub> multi-functional catalyst with high activity and stability for direct liquid fuel cells (DLFCs). *Sustain. Energy Fuels* **2021**, *5*, 4758–4770. [[CrossRef](#)]

59. Morka, T.D.; Ujihara, M. Enhanced performance of WO<sub>3</sub>/SnO<sub>2</sub> nanocomposite electrodes with redox-active electrolytes for supercapacitors. *Int. J. Mol. Sci.* **2023**, *24*, 6045. [[CrossRef](#)]
60. Shi, J.; Tian, X.D.; Wang, H.X.; Ge, L.; Li, J.F.; Lv, B.L. Oxygen deficient sea urchin-like Cu-WO<sub>3</sub> with high capacity and long life for anode of lithium-ion battery. *Appl. Surface Sci.* **2023**, *618*, 156627. [[CrossRef](#)]
61. Wang, J.Y.; Zhou, Y.R.; Zhao, W.X.; Niu, Y.T.; Mao, Y.L.; Cheng, W. Amorphous mixed-vanadium-tungsten oxide films as optically passive ion storage materials for solid-state near-infrared electrochromic devices. *ACS Appl. Mater. Interfaces* **2023**, *15*, 7120–7128. [[CrossRef](#)] [[PubMed](#)]
62. Wang, L.S.; Zhang, H.Y.; Yin, Y.L.; Zhou, Y.L.; Yin, X.X.; Wang, T.; Zeng, J.; Wang, W.K.; Zhou, W.C.; Tang, D.S. Controlled synthesis of 3D urchinlike niobium tungsten oxide nanostructure for fast hydrogen ion storage. *J. Phys. D Appl. Phys.* **2023**, *56*, 185501. [[CrossRef](#)]
63. Wu, C.; Shi, H.S.; Zhao, L.Q.; Chen, X.; Zhang, X.S.; Zhang, C.; Yu, J.M.; Lv, Y.J.; Wei, R.; Gao, T.Y.; et al. High-performance aqueous Zn<sup>2+</sup>/Al<sup>3+</sup> electrochromic batteries based on niobium tungsten oxides. *Adv. Funct. Mater.* **2023**, *33*, 2214886. [[CrossRef](#)]
64. Zou, Y.D.; Xi, S.B.; Bo, T.; Zhou, X.R.; Ma, J.H.; Yang, X.Y.; Diao, C.Z.; Deng, Y.H. Mesoporous amorphous Al<sub>2</sub>O<sub>3</sub>/crystalline WO<sub>3</sub> heterophase hybrids for electrocatalysis and gas sensing applications. *J. Mater. Chem. A* **2019**, *7*, 21874–21883. [[CrossRef](#)]
65. Mao, Y.; Wen, Y.; Chen, H.; Liao, M.; Zhang, F. Tungsten oxide flow sensor and its performance regulation. *IEEE Trans. Instrum. Meas.* **2022**, *71*, 9506608. [[CrossRef](#)]
66. Juang, F.-R.; Wang, W.-Y. Ethanol gas sensors with nanocomposite of nickel oxide and tungsten oxide. *IEEE Sens. J.* **2021**, *21*, 19740–19752. [[CrossRef](#)]
67. Drmosh, Q.A.; Al-Muhaish, N.A.; Al Wajih, Y.A.; Alam, M.W.; Yamani, Z.H. Surface composite and morphology tuning of tungsten oxide thin films for acetone gas sensing. *Chem. Phys. Lett.* **2021**, *776*, 138659. [[CrossRef](#)]
68. Ambardekar, V.; Bhowmick, T.; Bandyopadhyay, P.P. Understanding on the hydrogen detection of plasma sprayed tin oxide/tungsten oxide (SnO<sub>2</sub>/WO<sub>3</sub>) sensor. *Int. J. Hydrogen Energy* **2022**, *47*, 15120–15131. [[CrossRef](#)]
69. Mo, Y.S.; Feng, S.Q.; Yu, T.Q.; Chen, J.L.; Qian, G.F.; Luo, L.; Yin, S.B. Surface unsaturated WO<sub>x</sub> activating PtNi alloy nanowires for oxygen reduction reaction. *J. Colloid Interface Sci.* **2022**, *607*, 1928–1935. [[CrossRef](#)]
70. Tang, X.X.; Liu, J.L.; Zhan, K.; Sun, H.; Zhao, B.; Yan, Y. Molybdenum-tungsten oxide nanowires rich in oxygen vacancies as an advanced electrocatalyst for hydrogen evolution. *Chem. Asian J.* **2020**, *15*, 2984–2991. [[CrossRef](#)]
71. Li, Y.; Jiang, K.Y.; Yang, J.; Zheng, Y.Y.; Hubner, R.; Ou, Z.W.; Dong, X.; He, L.Q.; Wang, H.L.; Li, J.; et al. Tungsten oxide/reduced graphene oxide aerogel with low-content platinum as high-performance electrocatalyst for hydrogen evolution reaction. *Small* **2021**, *17*, 2102159. [[CrossRef](#)] [[PubMed](#)]
72. Peng, Q.M.; He, Q.T.; Hu, Y.; Isimjan, T.T.; Hou, R.B.; Yang, X.L. Interface engineering of porous Fe<sub>2</sub>P-WO<sub>2.92</sub> catalyst with oxygen vacancies for highly active and stable large-current oxygen evolution and overall water splitting. *J. Energy Chem.* **2022**, *65*, 574–582. [[CrossRef](#)]
73. Bharagav, U.; Reddy, N.R.; Koteswararao, V.N.; Ravi, P.; Pratap, K.; Sathish, M.; Cheralathan, K.K.; Shankar, M.V.; Kumari, M.M. Heterojunction of CdS Nanocapsules-WO<sub>3</sub> nanosheets composite as a stable and efficient photocatalyst for hydrogen evolution. *Energy Fuels* **2020**, *34*, 14598–14610. [[CrossRef](#)]
74. Nevolin, V.N.; Fominski, D.V.; Romanov, R.I.; Rubinkovskaya, O.V.; Soloviev, A.A.; Shvets, P.V.; Maznitsyna, E.A.; Fominski, V.Y. Influence of sulfidation conditions of WO<sub>3</sub> nanocrystalline film on photoelectrocatalytic activity of WS<sub>2</sub>/WO<sub>3</sub> hybrid structure in production of hydrogen. *Inorg. Mater. Appl. Res.* **2021**, *12*, 1139–1147. [[CrossRef](#)]
75. Sudha, A.; Koshy, A.M.; Swaminathan, P. Microstructure tailoring of tungsten oxide for enhanced properties by varying sintering temperatures. *Mater. Lett.* **2022**, *316*, 132007. [[CrossRef](#)]
76. Šedivá, R.; Pistonesi, C.; Proncato, M.E.; Duchoň, T.; Stetsovych, V.; Mysliveček, J.; Mašek, K. 1D tungsten oxide nanostructures on a Cu(1 1 0) surface. *J. Phys. Condens. Matter* **2018**, *30*, 465001. [[CrossRef](#)]
77. Dong, C.; Zhao, R.; Yao, L.; Ran, Y.; Zhang, X.; Wang, Y. A review on WO<sub>3</sub> based gas sensors: Morphology control and enhanced sensing properties. *J. Alloys Compd.* **2020**, *820*, 153194. [[CrossRef](#)]
78. Chen, B.; Laverock, J.; Piper, L.F.J.; Preston, A.R.H.; Cho, S.W.; DeMasi, A.; Smith, K.E.; Scanlon, D.O.; Watson, G.W.; Egdell, R.G.; et al. The band structure of WO<sub>3</sub> and non-rigid-band behaviour in Na<sub>0.67</sub>WO<sub>3</sub> derived from soft X-ray spectroscopy and density functional theory. *J. Phys. Condens. Matter* **2013**, *25*, 165501. [[CrossRef](#)]
79. Wang, F.; Di Valentin, C.; Pacchioni, G. Semiconductor-to-metal transition in WO<sub>3-x</sub>: Nature of the oxygen vacancy. *Phys. Rev. B* **2011**, *84*, 073103. [[CrossRef](#)]
80. Al Mohammad, A.; Gillet, M. Phase transformations in WO<sub>3</sub> thin films during annealing. *Thin Solid Films* **2002**, *408*, 302–309. [[CrossRef](#)]
81. Hernandez-Uresti, D.B.; Sánchez-Martínez, D.; Martínez-de la Cruz, A.; Sepúlveda-Guzmán, S.; Torres-Martínez, L.M. Characterization and photocatalytic properties of hexagonal and monoclinic WO<sub>3</sub> prepared via microwave-assisted hydrothermal synthesis. *Ceram. Int.* **2014**, *40*, 4767–4775. [[CrossRef](#)]
82. Nayak, A.K.; Verma, M.; Sohn, Y.; Deshpande, P.A.; Pradhan, D. Highly active tungsten oxide nanoplate electrocatalysts for the hydrogen evolution reaction in acidic and near neutral electrolytes. *ACS Omega* **2017**, *2*, 7039–7047. [[CrossRef](#)] [[PubMed](#)]
83. Ahmadi, M.; Sahoo, S.; Younesi, R.; Gaur, A.P.S.; Katiyar, R.S.; Guinel, M.J.F. WO<sub>3</sub> nano-ribbons: Their phase transformation from tungstite (WO<sub>3</sub> center dot H<sub>2</sub>O) to tungsten oxide (WO<sub>3</sub>). *J. Mater. Sci.* **2014**, *49*, 5899–5909. [[CrossRef](#)]

84. Sharma, L.; Kumar, P.; Halder, A. Phase and vacancy modulation in tungsten oxide: Electrochemical hydrogen evolution. *ChemElectroChem* **2019**, *6*, 3420–3428. [[CrossRef](#)]
85. Hajiahmadi, Z.; Azar, Y.T. Computational study of h-WO<sub>3</sub> surfaces as a semiconductor in water-splitting application. *Surf. Interfaces* **2022**, *28*, 101695. [[CrossRef](#)]
86. Mohamed, M.M.; Salama, T.M.; Hegazy, M.A.; Abou Shahba, R.M.; Mohamed, S.H. Synthesis of hexagonal WO<sub>3</sub> nanocrystals with various morphologies and their enhanced electrocatalytic activities toward hydrogen evolution. *Int. J. Hydrogen Energy* **2019**, *44*, 4724–4736. [[CrossRef](#)]
87. Ham, D.J.; Phuruangrat, A.; Thongtem, S.; Lee, J.S. Hydrothermal synthesis of monoclinic WO<sub>3</sub> nanoplates and nanorods used as an electrocatalyst for hydrogen evolution reactions from water. *Chem. Eng. J.* **2010**, *165*, 365–369. [[CrossRef](#)]
88. Zhou, H.W.; Shi, Y.T.; Dong, Q.S.; Lin, J.; Wang, A.Q.; Ma, T.L. Surface oxygen vacancy-dependent electrocatalytic activity of W<sub>18</sub>O<sub>49</sub> Nanowires. *J. Phys. Chem. C* **2014**, *118*, 20100–20106. [[CrossRef](#)]
89. Liang, H.F.; Cao, Z.; Xia, C.; Ming, F.W.; Zhang, W.L.; Emwas, A.H.; Cavallo, L.; Alshareef, H.N. Tungsten blue oxide as a reusable electrocatalyst for acidic water oxidation by plasma-induced vacancy engineering. *CCS Chem.* **2021**, *3*, 1553–1561. [[CrossRef](#)]
90. Sun, S.M.; Wu, J.; Watanabe, M.; Akbay, T.; Ishihara, T. Single-electron-trapped oxygen vacancy on ultrathin WO<sub>3</sub> center dot 0.33H<sub>2</sub>O {100} facets suppressing backward reaction for promoted H<sub>2</sub> evolution in pure water splitting. *J. Phys. Chem. Lett.* **2019**, *10*, 2998–3005. [[CrossRef](#)]
91. Wang, Y.; Wang, Y.; Bai, J.; Duan, S.; Wang, R.; Lau, W.-M. In-situ etching synthesis of 3D self-supported serrated Ni-WO<sub>3</sub> for oxygen evolution reaction. *J. Alloys Compd.* **2022**, *893*, 162134. [[CrossRef](#)]
92. Wu, X.; Zhang, T.; Wei, J.; Feng, P.; Yan, X.; Tang, Y. Facile synthesis of Co and Ce dual-doped Ni<sub>3</sub>S<sub>2</sub> nanosheets on Ni foam for enhanced oxygen evolution reaction. *Nano Res.* **2020**, *13*, 2130–2135. [[CrossRef](#)]
93. Hai, G.J.; Huang, J.F.; Cao, L.Y.; Kajiyoshi, K.; Wang, L.; Feng, L.L.; Chen, J. Activation of urchin-like Ni-doped W<sub>18</sub>O<sub>49</sub>/NF by electrochemical tuning for efficient water splitting. *J. Energy Chem.* **2021**, *63*, 642–650. [[CrossRef](#)]
94. Zheng, T.T.; Sang, W.; He, Z.H.; Wei, Q.S.; Chen, B.W.; Li, H.L.; Cao, C.; Huang, R.J.; Yan, X.P.; Pan, B.C.; et al. Conductive tungsten oxide nanosheets for highly efficient hydrogen evolution. *Nano Lett.* **2017**, *17*, 7968–7973. [[CrossRef](#)]
95. Chen, J.D.; Yu, D.N.; Liao, W.S.; Zheng, M.D.; Xiao, L.F.; Zhu, H.; Zhang, M.; Du, M.L.; Yao, J.M. WO<sub>3-x</sub> nanoplates grown on carbon nanofibers for an efficient electrocatalytic hydrogen evolution reaction. *ACS Appl. Mater. Interfaces* **2016**, *8*, 18132–18139. [[CrossRef](#)]
96. Li, Y.H.; Liu, P.F.; Pan, L.F.; Wang, H.F.; Yang, Z.Z.; Zheng, L.R.; Hu, P.; Zhao, H.J.; Gu, L.; Yang, H.G. Local atomic structure modulations activate metal oxide as electrocatalyst for hydrogen evolution in acidic water. *Nat. Commun.* **2015**, *6*, 8064. [[CrossRef](#)]
97. Li, D.X.; Xu, Y.; Lu, Y.L.; Chen, Y.Y.; Wu, Y.Y.; Yan, J.; Du, F.K.; Zhao, Y.Z.; Tan, X.C. Defect-rich engineering of Ni-incorporated tungsten oxides micro-flowers on carbon cloth: A binder-free electrode for highly efficient hydrogen evolution reaction. *J. Power Sources* **2022**, *520*, 230862–230870. [[CrossRef](#)]
98. Nayak, A.K.; Pradhan, D. Microwave-assisted greener synthesis of defect-rich tungsten oxide nanowires with enhanced photocatalytic and photoelectrochemical performance. *J. Phys. Chem. C* **2018**, *122*, 3183–3193. [[CrossRef](#)]
99. Xie, X.; Mu, W.J.; Li, X.L.; Wei, H.Y.; Jian, Y.; Yu, Q.H.; Zhang, R.; Lv, K.; Tang, H.; Luo, S.Z. Incorporation of tantalum ions enhances the electrocatalytic activity of hexagonal WO<sub>3</sub> nanowires for hydrogen evolution reaction. *Electrochim. Acta* **2014**, *134*, 201–208. [[CrossRef](#)]
100. Li, P.; Duan, X.; Kuang, Y.; Sun, X. Iridium in tungsten trioxide matrix as an efficient bi-functional electrocatalyst for overall water splitting in acidic media. *Small* **2021**, *17*, e2102078. [[CrossRef](#)]
101. Zhao, Y.; Lv, C.; Huang, Q.; Huang, Z.; Zhang, C. Self-supported tungsten/tungsten dioxide nanowires array as an efficient electrocatalyst in hydrogen evolution reaction. *RSC Adv.* **2016**, *6*, 89815–89820. [[CrossRef](#)]
102. Rajalakshmi, R.; Viswanathan, C.; Ponpandian, N. Sm<sup>3+</sup> rare-earth doping in non-noble metal oxide-WO<sub>3</sub> grown on carbon cloth fibre as a bifunctional electrocatalyst for high-performance water electrolysis. *Sustain. Energy Fuels* **2021**, *5*, 5851–5865. [[CrossRef](#)]
103. Ma, J.W.; Ma, Z.R.; Liu, B.B.; Wang, S.; Ma, R.X.; Wang, C.Y. Composition of Ag-WO<sub>3</sub> core-shell nanostructures as efficient electrocatalysts for hydrogen evolution reaction. *J. Solid State Chem.* **2019**, *271*, 246–252. [[CrossRef](#)]
104. Wang, D.L.; Li, H.P.; Du, N.; Hou, W.G. Single platinum atoms immobilized on monolayer tungsten trioxide nanosheets as an efficient electrocatalyst for hydrogen evolution reaction. *Adv. Funct. Mater.* **2021**, *31*, 2009770. [[CrossRef](#)]
105. Liu, J.C.; Tang, C.Y.; Ke, Z.J.; Chen, R.; Wang, H.B.; Li, W.Q.; Jiang, C.Z.; He, D.; Wang, G.M.; Xiao, X.H. Optimizing hydrogen adsorption by d-d orbital modulation for efficient hydrogen evolution catalysis. *Adv. Energy Mater.* **2022**, *12*, 2103301. [[CrossRef](#)]
106. Sun, X.; Yang, F.; Liu, Z.; Zeng, L.; Cui, X. Fabrication of Fe and P Co-doped WO<sub>2</sub> nano-polygonal pyramid as an efficient electrocatalyst for hydrogen evolution reaction. *Chem. Lett.* **2019**, *48*, 1232–1235. [[CrossRef](#)]
107. Yue, X.; Zheng, Y.; Chen, Y.; Huang, S. Overall water splitting on Ni<sub>0.19</sub>WO<sub>4</sub> nanowires as highly efficient and durable bifunctional non-precious metal electrocatalysts. *Electrochim. Acta* **2020**, *333*, 135554. [[CrossRef](#)]
108. Jiang, D.L.; Xu, S.J.; Gao, M.H.; Lu, Y.K.; Liu, Y.; Sun, S.C.; Di, L. Synergistically integrating nickel porous nanosheets with 5d transition metal oxides enabling efficient electrocatalytic overall water splitting. *Inorg. Chem.* **2021**, *60*, 8189–8199. [[CrossRef](#)]
109. Peng, C.L.; Zhao, W.P.; Kuang, Z.Y.; Miller, J.T.; Chen, H.R. Boosting neutral hydrogen evolution reaction on iridium by support effect of W<sub>18</sub>O<sub>49</sub>. *Appl. Catal. A-Gen.* **2021**, *623*, 9. [[CrossRef](#)]
110. Wang, C.Z.; Wang, R.; Peng, Y.; Chen, J.N.; Li, J.H. Iron tungsten mixed composite as a robust oxygen evolution electrocatalyst. *Chem. Comm.* **2019**, *55*, 10944–10947. [[CrossRef](#)]

111. Xi, Z.; Mendoza-Garcia, A.; Zhu, H.Y.; Chi, M.F.; Su, D.; Erdosy, D.P.; Li, J.R.; Sun, S.H. Ni<sub>x</sub>WO<sub>2.72</sub> nanorods as an efficient electrocatalyst for oxygen evolution reaction. *Green Energy Environ.* **2017**, *2*, 119–123. [[CrossRef](#)]
112. Park, J.; Lee, S.; Kim, H.E.; Cho, A.; Kim, S.; Ye, Y.; Han, J.W.; Lee, H.; Jang, J.H.; Lee, J. Investigation of the support effect in atomically dispersed Pt on WO<sub>3-x</sub> for utilization of Pt in the hydrogen evolution reaction. *Angew. Chem. Int. Ed.* **2019**, *58*, 16038–16042. [[CrossRef](#)] [[PubMed](#)]
113. Peng, L.; Su, L.; Yu, X.; Wang, R.; Cui, X.; Tian, H.; Cao, S.; Xia, B.Y.; Shi, J. Electron redistribution of ruthenium-tungsten oxides Mott-Schottky heterojunction for enhanced hydrogen evolution. *Appl. Catal. B—Environ.* **2022**, *308*, 121229. [[CrossRef](#)]
114. Ren, Y.M.; Chen, Z.H.; Yu, X.R. Ultrathin, porous and oxygen vacancies-enriched Ag/WO<sub>3-x</sub> heterostructures for electrocatalytic hydrogen evolution. *Chem.-Asian J.* **2019**, *14*, 4315–4321. [[CrossRef](#)] [[PubMed](#)]
115. Zhong, X.; Sun, Y.; Chen, X.; Zhuang, G.; Li, X.; Wang, J.-G. Mo doping induced more active sites in urchin-like W<sub>18</sub>O<sub>49</sub> nanostructure with remarkably enhanced performance for hydrogen evolution reaction. *Adv. Funct. Mater.* **2016**, *26*, 5778–5786. [[CrossRef](#)]
116. Hu, W.; Tian, M.; Zeng, K.; Yan, J.; Zhou, J.; Zhang, J.; Rummeli, M.H.; Wang, H.; Yang, R. Tuning the electronic structure of W<sub>18</sub>O<sub>49</sub> via dual doping for efficient oxygen evolution reaction. *ACS Appl. Energy Mater.* **2022**, *5*, 3208–3216. [[CrossRef](#)]
117. Zhao, Y.; Tang, Q.; Yang, P.; He, B. Robust electrocatalysts from metal doped W<sub>18</sub>O<sub>49</sub> nanofibers for hydrogen evolution. *Chem. Comm.* **2017**, *53*, 4323–4326. [[CrossRef](#)]
118. Zhao, Y.Y.; Tang, Q.W.; He, B.L.; Yang, P.Z. Mo incorporated W<sub>18</sub>O<sub>49</sub> nanofibers as robust electrocatalysts for high-efficiency hydrogen evolution. *Int. J. Hydrogen Energy* **2017**, *42*, 14534–14546. [[CrossRef](#)]
119. Nakayama, M.; Takeda, A.; Maruyama, H.; Kumbhar, V.; Crosnier, O. Cobalt-substituted iron-based wolframite synthesized via polyol route for efficient oxygen evolution reaction. *Electrochem. Commun.* **2020**, *120*, 106834–106840. [[CrossRef](#)]
120. Tian, H.; Cui, X.Z.; Zeng, L.M.; Su, L.; Song, Y.L.; Shi, J.L. Oxygen vacancy-assisted hydrogen evolution reaction of the Pt/WO<sub>3</sub> electrocatalyst. *J. Mater. Chem. A* **2019**, *7*, 6285–6293. [[CrossRef](#)]
121. Shu, C.; Kang, S.; Jin, Y.S.; Yue, X.; Shen, P.K. Bifunctional porous non-precious metal WO<sub>2</sub> hexahedral networks as an electrocatalyst for full water splitting. *J. Mater. Chem. A* **2017**, *5*, 9655–9660. [[CrossRef](#)]
122. Song, J.; Huang, Z.-F.; Pan, L.; Zou, J.-J.; Zhang, X.; Wang, L. Oxygen-deficient tungsten oxide as versatile and efficient hydrogenation catalyst. *ACS Catal.* **2015**, *5*, 6594–6599. [[CrossRef](#)]
123. Zheng, X.; Chen, Y.; Bao, X.; Mao, S.; Fan, R.; Wang, Y. In situ formed bimetallic carbide Ni<sub>6</sub>Mo<sub>6</sub>C nanodots and NiMoO<sub>x</sub> nanosheet array hybrids anchored on carbon cloth: Efficient and flexible self-supported catalysts for hydrogen evolution. *ACS Catal.* **2020**, *10*, 11634–11642. [[CrossRef](#)]
124. Zhang, J.; Qian, J.; Ran, J.; Xi, P.; Yang, L.; Gao, D. Engineering lower coordination atoms onto NiO/Co<sub>3</sub>O<sub>4</sub> heterointerfaces for boosting oxygen evolution reactions. *ACS Catal.* **2020**, *10*, 12376–12384. [[CrossRef](#)]
125. Duan, Y.; Yu, Z.Y.; Hu, S.J.; Zheng, X.S.; Zhang, C.T.; Ding, H.H.; Hu, B.C.; Fu, Q.Q.; Yu, Z.L.; Zheng, X.; et al. Scaled-up synthesis of amorphous NiFeMo oxides and their rapid surface reconstruction for superior oxygen evolution catalysis. *Angew. Chem.* **2019**, *58*, 15772–15777. [[CrossRef](#)] [[PubMed](#)]
126. Miao, X.; Wu, L.; Lin, Y.; Yuan, X.; Zhao, J.; Yan, W.; Zhou, S.; Shi, L. The role of oxygen vacancies in water oxidation for perovskite cobalt oxide electrocatalysts: Are more better? *Chem. Comm.* **2019**, *55*, 1442–1445. [[CrossRef](#)]
127. Guo, C.; Liu, X.; Gao, L.; Ma, X.; Zhao, M.; Zhou, J.; Kuang, X.; Deng, W.; Sun, X.; Wei, Q. Oxygen defect engineering in cobalt iron oxide nanosheets for promoted overall water splitting. *J. Mater. Chem. A* **2019**, *7*, 21704–21710. [[CrossRef](#)]
128. Cai, Z.; Bi, Y.; Hu, E.; Liu, W.; Dwarica, N.; Tian, Y.; Li, X.; Kuang, Y.; Li, Y.; Yang, X.-Q.; et al. Single-crystalline ultrathin Co<sub>3</sub>O<sub>4</sub> nanosheets with massive vacancy defects for enhanced electrocatalysis. *Adv. Energy Mater.* **2018**, *8*, 1701694. [[CrossRef](#)]
129. Qiao, D.; Wang, Y.; Li, F.; Wang, D.Y.; Yan, B.J. Kinetic study on preparation of substoichiometric tungsten oxide WO<sub>2.72</sub> via hydrogen reduction process. *J. Therm. Anal. Calorim.* **2019**, *137*, 389–397. [[CrossRef](#)]
130. Wang, Z.; Zhang, Y.; Neyts, E.C.; Cao, X.; Zhang, X.; Jang, B.W.L.; Liu, C.-j. Catalyst preparation with plasmas: How does it work? *ACS Catal.* **2018**, *8*, 2093–2110. [[CrossRef](#)]
131. Xu, L.; Jiang, Q.; Xiao, Z.; Li, X.; Huo, J.; Wang, S.; Dai, L. Plasma-engraved Co<sub>3</sub>O<sub>4</sub> nanosheets with oxygen vacancies and high surface area for the oxygen evolution reaction. *Angew. Chem.* **2016**, *128*, 5363–5367. [[CrossRef](#)]
132. Anis, S.F.; Lalia, B.S.; Mostafa, A.O.; Hashaikeh, R. Electrospun nickel-tungsten oxide composite fibers as active electrocatalysts for hydrogen evolution reaction. *J. Mater. Sci.* **2017**, *52*, 7269–7281. [[CrossRef](#)]
133. Lu, K.; Wang, Z.; Wu, Y.; Zhai, X.; Wang, C.; Li, J.; Wang, Z.; Li, X.; He, Y.; An, T.; et al. Synergistic effect of F doping and WO<sub>3</sub> loading on electrocatalytic oxygen evolution. *Chem. Eng. J.* **2023**, *451*, 138590. [[CrossRef](#)]
134. Xu, H.; Zhao, Y.; He, G.; Chen, H. Race on engineering noble metal single-atom electrocatalysts for water splitting. *Int. J. Hydrogen Energy* **2022**, *47*, 14257–14279. [[CrossRef](#)]
135. Tomboc, G.M.; Kim, T.; Jung, S.; Yoon, H.J.; Lee, K. Modulating the local coordination environment of single-atom catalysts for enhanced catalytic performance in hydrogen/oxygen evolution reaction. *Small* **2022**, *18*, 2105680. [[CrossRef](#)]
136. Li, J.C.; Zhang, C.; Zhang, C.; Ma, H.J.; Yang, Y.; Guo, Z.Q.; Wang, Y.Y.; Ma, H.X. Electronic configuration of single ruthenium atom immobilized in urchin-like tungsten trioxide towards hydrazine oxidation-assisted hydrogen evolution under wide pH media. *Chem. Eng. J.* **2022**, *430*, 132953–132965. [[CrossRef](#)]
137. Xu, W.; Ni, X.M.; Zhang, L.J.; Yang, F.; Peng, Z.; Huang, Y.F.; Liu, Z. Tuning the electronic structure of tungsten oxide for enhanced hydrogen evolution reaction in alkaline electrolyte. *ChemElectroChem* **2022**, *9*, e202101300. [[CrossRef](#)]

138. Liu, L.; Zhao, Y.Z.; Wang, Y.; Zhang, Z.L.; Liu, J.; Wu, T.; Qin, W.J.; Liu, S.J.; Jia, B.R.; Wu, H.Y.; et al. Single-atom Co doped in ultrathin WO<sub>3</sub> arrays for the enhanced hydrogen evolution reaction in a wide pH range. *ACS Appl. Mater. Interfaces* **2021**, *13*, 53915–53924. [[CrossRef](#)]
139. Zhang, H.; Li, X.; Hähnel, A.; Naumann, V.; Lin, C.; Azimi, S.; Schweizer, S.L.; Maijenburg, A.W.; Wehrspohn, R.B. Bifunctional heterostructure assembly of NiFe LDH nanosheets on NiCoP nanowires for highly efficient and stable overall water splitting. *Adv. Funct. Mater.* **2018**, *28*, 1706847. [[CrossRef](#)]
140. Ngo, Y.-L.T.; Bhamu, K.C.; Voronova, A.; Jana, J.; Kang, S.G.; Chung, J.S.; Choi, W.M.; Jang, J.H.; Hur, S.H.; Seo, B. Carbide-directed enhancement of electrochemical hydrogen evolution reaction on tungsten carbide-oxide heterostructure. *Chem. Eng. J.* **2022**, *450*, 137915. [[CrossRef](#)]
141. Yang, L.; Zhu, X.B.; Xiong, S.J.; Wu, X.L.; Shan, Y.; Chu, P.K. Synergistic WO<sub>3</sub> center dot 2H<sub>2</sub>O nanoplates/WS<sub>2</sub> hybrid catalysts for high-efficiency hydrogen evolution. *ACS Appl. Mater. Interfaces* **2016**, *8*, 13966–13972. [[CrossRef](#)] [[PubMed](#)]
142. Wu, R.; Zhang, J.F.; Shi, Y.M.; Liu, D.; Zhang, B. Metallic WO<sub>2</sub>-carbon mesoporous nanowires as highly efficient electrocatalysts for hydrogen evolution reaction. *J. Am. Chem. Soc.* **2015**, *137*, 6983–6986. [[CrossRef](#)] [[PubMed](#)]
143. Sekar, S.; Ahmed, A.A.; Pawar, S.M.; Lee, Y.; Im, H.; Kim, D.Y.; Lee, S. Enhanced water splitting performance of biomass activated carbon-anchored WO<sub>3</sub> nanoflakes. *Appl. Surf. Sci.* **2020**, *508*, 145127. [[CrossRef](#)]
144. Hu, G.J.; Li, J.; Liu, P.; Zhu, X.Q.; Li, X.F.; Ali, R.N.; Xiang, B. Enhanced electrocatalytic activity of WO<sub>3</sub>@NPRGO composite in a hydrogen evolution reaction. *Appl. Surf. Sci.* **2019**, *463*, 275–282. [[CrossRef](#)]
145. Peng, X.; Nie, X.; Zhang, L.; Liang, T.; Liu, Y.; Liu, P.; Men, Y.L.; Niu, L.; Zhou, J.; Cui, D.; et al. Carbon-coated tungsten oxide nanospheres triggering flexible electron transfer for efficient electrocatalytic oxidation of water and glucose. *ACS Appl. Mater. Interfaces* **2020**, *12*, 56943–56953. [[CrossRef](#)]
146. Wondimu, T.H.; Chen, G.C.; Chen, H.Y.; Kabtamu, D.M.; Bayeh, A.W.; Wang, K.C.; Huang, H.C.; Wang, C.H. High catalytic activity of oxygen-vacancy-rich tungsten oxide nanowires supported by nitrogen-doped reduced graphene oxide for the hydrogen evolution reaction. *J. Mater. Chem. A* **2018**, *6*, 19767–19774. [[CrossRef](#)]
147. Liu, C.H.; Qiu, Y.Y.; Xia, Y.J.; Wang, F.; Liu, X.C.; Sun, X.H.; Liang, Q.; Chen, Z.D. Noble-metal-free tungsten oxide/carbon (WO<sub>x</sub>/C) hybrid nanowires for highly efficient hydrogen evolution. *Nanotechnology* **2017**, *28*, 445403. [[CrossRef](#)]
148. Anupama, V.R.; Mideen, A.S.; Shibli, S.M.A. Tuning of electrocatalytic activity of WO<sub>3</sub>-TiO<sub>2</sub> nanocomposite electrode for alkaline hydrogen evolution reaction. *Int. J. Hydrogen Energy* **2021**, *46*, 15145–15160. [[CrossRef](#)]
149. Shang, X.; Rao, Y.; Lu, S.S.; Dong, B.; Zhang, L.M.; Liu, X.H.; Li, X.; Liu, Y.R.; Chai, Y.M.; Liu, C.G. Novel WS<sub>2</sub>/WO<sub>3</sub> heterostructured nanosheets as efficient electrocatalyst for hydrogen evolution reaction. *Mater. Chem. Phys.* **2017**, *197*, 123–128. [[CrossRef](#)]
150. Han, C.; Wang, D.; Li, Q.; Xing, Z.; Yang, X. Ni<sub>17</sub>W<sub>3</sub> nanoparticles decorated WO<sub>2</sub> nanohybrid electrocatalyst for highly efficient hydrogen evolution reaction. *ACS Appl. Energy Mater.* **2019**, *2*, 2409–2413. [[CrossRef](#)]
151. Wang, B.Z.; Wang, L.X.; Qian, Y.T.; Yang, Y.T.; Isimjan, T.T.; Yang, X.L. Construction of a self-supporting Ni<sub>2</sub>P-WO<sub>3</sub> heterostructure for highly efficient hydrogen evolution under both caustic and acidic conditions. *Sustain. Energy Fuels* **2021**, *5*, 2884–2892. [[CrossRef](#)]
152. Xu, W.; Wang, B.B.; Ni, X.M.; Liu, H.Y.; Wang, W.; Zhang, L.J.; Zhang, H.; Peng, Z.; Liu, Z. Heterogeneous synergetic effect of metal-oxide interfaces for efficient hydrogen evolution in alkaline solutions. *ACS Appl. Mater. Interfaces* **2021**, *13*, 13838–13847. [[CrossRef](#)] [[PubMed](#)]
153. Liu, X.N.; Wang, C.W. In situ wet etching of MoS<sub>2</sub>@dWO<sub>3</sub> Heterostructure as ultra-stable highly active electrocatalyst for hydrogen evolution reaction. *Catalysts* **2020**, *10*, 977. [[CrossRef](#)]
154. Lv, C.; Yan, G.; Wang, X.; Gao, L.; Xu, S.; San, X.; Wang, S.; Li, Y.; Huang, Z. Ni loaded on N-doped carbon encapsulated tungsten oxide nanowires as an alkaline-stable electrocatalyst for water reduction. *Sustain. Energy Fuels* **2020**, *4*, 788–796. [[CrossRef](#)]
155. Wang, X.; Gan, X.; Hu, T.; Fujisawa, K.; Lei, Y.; Lin, Z.; Xu, B.; Huang, Z.H.; Kang, F.; Terrones, M.; et al. Noble-metal-free hybrid membranes for highly efficient hydrogen evolution. *Adv. Mater.* **2017**, *29*, 1603617. [[CrossRef](#)]
156. Gong, F.L.; Yao, C.J.; Kong, H.J.; Meng, E.C.; Gong, L.H.; Zhang, Y.H.; Li, F. WO<sub>3</sub>/C nanoarchitectures assembled with 1D nanowires: The synthesis, Pt nanoparticles decoration, and highly enhanced hydrogen evolution in neutral media. *J. Phys. Chem. Solids* **2022**, *163*, 110542. [[CrossRef](#)]
157. Jiang, X.L.; Jang, H.S.; Liu, S.G.; Li, Z.J.; Kim, M.G.; Li, C.; Qin, Q.; Liu, X.; Cho, J. The heterostructure of Ru<sub>2</sub>P/WO<sub>3</sub>/NPC synergistically promotes H<sub>2</sub>O dissociation for improved hydrogen evolution. *Angew. Chem. Int. Ed.* **2021**, *60*, 4110–4116. [[CrossRef](#)]
158. Jiang, W.J.; Chen, J.L.; Qian, G.F.; He, H.B.; Zhang, H.; Zhuo, X.Y.; Shen, F.; Luo, L.; Yin, S.B. Interfacial electronic engineering of carbon encapsulated Co<sub>5.47</sub>N-WO<sub>2</sub> for boosting overall water splitting. *Electrochim. Acta* **2021**, *390*, 138887. [[CrossRef](#)]
159. Lv, Y.; Liu, Y.; Liu, Y.K.; Chen, Z.; Zhang, M. CoSe<sub>2</sub>/WSe<sub>2</sub>/WO<sub>3</sub> hybrid nanowires on carbon cloth for efficient hydrogen evolution reaction. *J. Alloys Compd.* **2018**, *768*, 889–895. [[CrossRef](#)]
160. Yang, Y.T.; Shao, X.; Zhou, S.Q.; Yan, P.X.; Isimjan, T.T.; Yang, X.L. Interfacial electronic coupling of NC@WO<sub>3</sub>-W<sub>2</sub>C decorated Ru clusters as a reversible catalyst toward electrocatalytic hydrogen oxidation and evolution reactions. *ChemSusChem* **2021**, *14*, 2992–3000. [[CrossRef](#)]
161. Chen, Y.T.; Ren, R.; Wen, Z.H.; Ci, S.Q.; Chang, J.B.; Mao, S.; Chen, J.H. Superior electrocatalysis for hydrogen evolution with crumpled graphene/tungstendisulfide/tungsten trioxide ternary nanohybrids. *Nano Energy* **2018**, *47*, 66–73. [[CrossRef](#)]

162. Yang, N.N.; Chen, Z.G.; Ding, D.; Zhu, C.F.; Gan, X.X.; Cui, Y. Tungsten-nickel alloy boosts alkaline hydrogen evolution reaction. *J. Phys. Chem. C* **2021**, *125*, 27185–27191. [[CrossRef](#)]
163. Peng, Y.W.; Shan, C.; Wang, H.J.; Hong, L.Y.; Yao, S.; Wu, R.J.; Zhang, Z.M.; Lu, T.B. Polyoxometalate-derived ultrasmall Pt<sub>2</sub>W/WO<sub>3</sub> heterostructure outperforms platinum for large-current-density H<sub>2</sub> evolution. *Adv. Energy Mater.* **2019**, *9*, 1900597. [[CrossRef](#)]
164. Kim, D.; Jeong, Y.; Roh, H.; Lim, C.; Yong, K. Biomimetic 2D-Ni(Co,Fe)P/1D-WO<sub>x</sub> nanocoral reef electrocatalysts for efficient water splitting. *J. Mater. Chem. A* **2021**, *9*, 10909–10920. [[CrossRef](#)]
165. Noh, S.; Le, T.H.; Jo, H.; Kim, S.; Yoon, H. Ternary nanohybrids comprising N-doped graphene and WSe<sub>2</sub>-WO<sub>3</sub> nanosheets enable high-mass-loading electrodes with long-term stability for hydrogen evolution. *ACS Appl. Nano Mater.* **2021**, *4*, 14094–14104. [[CrossRef](#)]
166. Liu, J.C.; Qian, G.F.; Zhang, H.; Chen, J.L.; Wang, Y.J.; He, H.B.; Luo, L.; Yin, S.B. Amorphous FeOOH coating stabilizes WO<sub>2</sub>-Na<sub>x</sub>WO<sub>3</sub> for accelerating oxygen evolution reaction. *Chem. Eng. J.* **2021**, *426*, 131253. [[CrossRef](#)]
167. Wang, Y.; Wang, Y.; Bai, J.; Duan, S.; Wang, R.; Lau, W.-M. Fe ion-chelated tannic acid layer coordinates the electronic structure of Ni-WO<sub>x</sub> to enhance oxygen evolution performance. *J. Alloys Compd.* **2022**, *928*, 167225. [[CrossRef](#)]
168. Wondimu, T.H.; Chen, G.C.; Kabtamu, D.M.; Chen, H.Y.; Bayeh, A.W.; Huang, H.C.; Wang, C.H. Highly efficient and durable phosphine reduced iron-doped tungsten oxide/reduced graphene oxide nanocomposites for the hydrogen evolution reaction. *Int. J. Hydrogen Energy* **2018**, *43*, 6481–6490. [[CrossRef](#)]
169. Zhu, M.; Sun, J.; Li, C.; Han, C.; Shan, Y.; He, J.; Jia, J.; Wu, W.; Yang, G. Electrospun SiO<sub>2</sub>/WO<sub>3</sub>/NiWO<sub>4</sub> decorated carbon nanofibers for an efficient electrocatalytic hydrogen evolution. *Fuller. Nanotub. Carbon Nanostruct.* **2019**, *27*, 506–513. [[CrossRef](#)]
170. Nguyen, T.V.; Do, H.H.; Tekalgne, M.; Le, Q.V.; Nguyen, T.P.; Hong, S.H.; Cho, J.H.; Dao, D.V.; Ahn, S.H.; Kim, S.Y. WS<sub>2</sub>-WC-WO<sub>3</sub> nano-hollow spheres as an efficient and durable catalyst for hydrogen evolution reaction. *Nano Converg.* **2021**, *8*, 28. [[CrossRef](#)]
171. Zhang, B.; Hou, J.G.; Wu, Y.Z.; Cao, S.Y.; Li, Z.W.; Nie, X.W.; Gao, Z.M.; Sun, L.C. Tailoring active sites in mesoporous defect-rich NC/V<sub>o</sub>-WON heterostructure array for superior electrocatalytic hydrogen evolution. *Adv. Energy Mater.* **2019**, *9*, 1803693–1803702. [[CrossRef](#)]
172. Wang, Z.; Lin, Z.; Shen, S.; Zhong, W.; Cao, S. Advances in designing heterojunction photocatalytic materials. *Chin. J. Catal.* **2021**, *42*, 710–730. [[CrossRef](#)]
173. Wu, Z.; Liu, B.; Jing, H.; Gao, H.; He, B.; Xia, X.; Lei, W.; Hao, Q. Porous carbon framework decorated with carbon nanotubes encapsulating cobalt phosphide for efficient overall water splitting. *J. Colloid Interface Sci.* **2023**, *629*, 22–32. [[CrossRef](#)]
174. Zhang, Y.; Chen, L.; Yan, B.; Zhang, F.; Shi, Y.; Guo, X. Regeneration of textile sludge into Cu<sub>8</sub>S<sub>5</sub> decorated N, S self-doped interconnected porous carbon as an advanced bifunctional electrocatalyst for overall water splitting. *Chem. Eng. J.* **2023**, *451*, 138497. [[CrossRef](#)]
175. Wang, Q.; Yu, R.; Shen, D.; Liu, Q.; Hong Luo, K.; Wu, C.; Gu, S. Performance of intrinsic heteroatoms in cobalt phosphide loaded ginkgo leaf-based carbon material on promoting the electrocatalytic activity during hydrogen evolution reaction and oxygen evolution reaction. *Fuel* **2023**, *333*, 126368. [[CrossRef](#)]
176. Liu, J.; Zhang, J.; Zhou, H.; Liu, B.; Dong, H.; Lin, X.; Qin, Y. Lignin-derived carbon-supported MoC-FeNi heterostructure as efficient electrocatalysts for oxygen evolution reaction. *J. Colloid Interface Sci.* **2023**, *629*, 822–831. [[CrossRef](#)]
177. Chen, J.; Yang, H.; Sang, X.; Su, Z.; Li, D.; Wang, Q. Oxygen vacancy rich tungsten oxide with nitrogen doped mesoporous carbon as matrix for overall water splitting and 4-nitrophenol reductive removal. *Solid State Sci.* **2018**, *83*, 23–30. [[CrossRef](#)]
178. Jing, S.; Lu, J.; Yu, G.; Yin, S.; Luo, L.; Zhang, Z.; Ma, Y.; Chen, W.; Shen, P.K. Carbon-encapsulated WO<sub>x</sub> hybrids as efficient catalysts for hydrogen evolution. *Adv. Mater.* **2018**, *30*, e1705979. [[CrossRef](#)]
179. Lu, J.J.; Qian, G.F.; Luo, L.; He, H.B.; Yin, S.B. Contributions of oxygen vacancies to the hydrogen evolution catalytic activity of tungsten oxides. *Int. J. Hydrogen Energy* **2021**, *46*, 676–682. [[CrossRef](#)]

**Disclaimer/Publisher's Note:** The statements, opinions and data contained in all publications are solely those of the individual author(s) and contributor(s) and not of MDPI and/or the editor(s). MDPI and/or the editor(s) disclaim responsibility for any injury to people or property resulting from any ideas, methods, instructions or products referred to in the content.